

LA-UR-21-32430

Approved for public release; distribution is unlimited.

Title: Intentional Uranium Tagging for Material Provenance and Pathway Forensics (LA19-Intentional-Forensics-NDD3Bb): Annual Report for FY21

Author(s): Hackenberg, Robert Errol; Luitjohan, Kara Eileen; O'Brien, Lindsay Beth; Black, Amber Nalani; Bloom, Rose Anne; Imhoff, Seth D.; Montgomery, Colt James; Tegtmeier, Eric Lee; Winter, William Paul III

Intended for: Report

Issued: 2021-12-21



Los Alamos National Laboratory, an affirmative action/equal opportunity employer, is operated by Triad National Security, LLC for the National Nuclear Security Administration of U.S. Department of Energy under contract 89233218CNA000001. By approving this article, the publisher recognizes that the U.S. Government retains nonexclusive, royalty-free license to publish or reproduce the published form of this contribution, or to allow others to do so, for U.S. Government purposes. Los Alamos National Laboratory requests that the publisher identify this article as work performed under the auspices of the U.S. Department of Energy. Los Alamos National Laboratory strongly supports academic freedom and a researcher's right to publish; as an institution, however, the Laboratory does not endorse the viewpoint of a publication or guarantee its technical correctness.

Intentional Uranium Tagging for Material Provenance and Pathway Forensics (LA19-Intentional-Forensics-NDD3Bb): Annual Report for FY21

Robert E. Hackenberg, Kara E. Luitjohan, Lindsay B. O'Brien, Amber N. Black, Rose A. Bloom,
Seth D. Imhoff, Colt J. Montgomery, Eric L. Tegtmeier, William P. Winter III

Sigma Manufacturing Sciences Division
Los Alamos National Laboratory

December 2021

LA-UR-21-

ABSTRACT

This report describes the outcomes of the third and final year of a project to research the feasibility of tagging uranium materials, especially nuclear fuels. The experimental focus remained on metallic uranium forms under prospective surface and bulk tagging scenarios. Overall, the results showed that the tags could be successfully imparted and characterized in both as-built and degraded conditions. This was in line with expectations coming into this project, indicating promise for both surface and bulk tagging of metallic forms of uranium.

Multiple surface tagging techniques and detection strategies were explored in FY21, with an emphasis on improving tag quality, readability, and detection in the field. Non-radioactive materials were used as a testbed. Selective deposition via laser beam was determined to be successful in imparting a readable titanium deposit on a stainless steel base plate, and can be read with high resolution characterization techniques (e.g., scanning electron microscopy) and field capable tools (e.g., eddy current testing). Other deposition techniques, such as selective deposition via electron beam and photoluminescent tags, were explored in FY21, and while success for these techniques would be dependent on additional work, these techniques showed potential for surface tagging applications.

To survey bulk taggant elements for bulk uranium metal, 16 tagging elements were spread among 18 depleted uranium castings (4 baseline, 3 mix, 1 dilution, and 10 recycle). Most of these were made and characterized in FY21. Taggant acceptability was based upon manufacturability, detectability, and persistence from the standpoint of two detection options: bulk chemical analysis (for “chemical taggants”) and microstructural analysis (for “second phase taggants”). Taggant detection in both up-front manufacturing and in the face of “degradations” such as dilution, mixing, and recycling was generally good. Two independent laboratories carried out chemical analysis on most of the castings, and often at several locations within a casting, and the results are discussed. Scanning electron microscopy+EDS microanalysis revealed the second phases mostly contained the expected tagging elements. The shapes and

spatial distributions of these micron-sized carbides, oxides, and intermetallic particles offers opportunities for further science-based investigation and tagging optimization. Overall, V and Co currently appear as the best choices for chemical taggants while Al, Ti, Mn, Co, Pd, and Tb all look good as second phase taggants. The other elements considered here – Sc, Ni, Ge, Nb, Ce, Ta, W, Ir, and Au – while not being ruled out, require more study to become viable options. It is of special note that in the recycling study only one of the 12 elements fell out of detection even after 10 meltings, demonstrating their persistence.

An Appendix tabulates all chemical analysis results to enable more quantitative and statistical studies of detection opportunities and limitations, as a part of a related project.

CONTENTS

LIST OF ACRONYMS AND SYMBOLS

- 1. INTRODUCTION**
 - 1.1. Mission relevance, goals and impact**
 - 1.2. Overview of FY21 activities and structure of this report**
- 2. TASK B. SURFACE TAGGING**
 - 2.1. Previous results and discussion**
 - 2.2. Current results and discussion**
 - 2.2.1. Review of current (FY21) work)
 - 2.2.2. Electron beam deposition
 - 2.2.3. Laser beam deposition
 - 2.2.3.1 Characterization and results from FY20 signatures
 - 2.2.3.2 Characterization (using XRF, EC, and EDS) and results from FY21 signatures
 - 2.2.4. PFIB signature results
 - 2.2.5. Literature review of photoluminescence
 - 2.3. Surface tagging conclusions**
- 3. TASK C. BULK URANIUM METAL TAGGING**
 - 3.1. Summary of technical approach**
 - 3.2. Activity overview**
 - 3.2.1. Casting and sampling
 - 3.2.2. Bulk chemical analysis
 - 3.2.3. Microscopy
 - 3.3. Review of prior (FY19, FY20) work**
 - 3.3.1. Baseline alloys: design and procedure
 - 3.3.2. Baseline alloys: chemistry results
 - 3.3.3. Baseline alloys: microscopy results
 - 3.4. FY21 activity – baseline alloys**
 - 3.4.1. Addition of elements in specific ratios – chemistry results
 - 3.4.2. Secondary phase segregation – microscopy results
 - 3.4.3. Conclusions – baseline alloys
 - 3.5. FY21 activity – mixed/dilution alloys**
 - 3.5.1. Design and procedure
 - 3.5.2. Casting outcomes
 - 3.5.3. Addition of elements in specific ratios – chemistry results
 - 3.5.4. Secondary phase segregation – microscopy results
 - 3.5.5. Conclusions – mixed/dilution alloys
 - 3.6. FY21 activity – recycling study**
 - 3.6.1. Design and procedure
 - 3.6.2. Retention of elements – chemistry results
 - 3.6.3. Conclusions – recycling study
 - 3.7. Bulk metal tagging conclusions**

ACKNOWLEDGEMENTS

REFERENCES

APPENDIX: Chemical analysis results for the 18 bulk tagging alloys

LIST OF ACRONYMS AND SYMBOLS

BSE	back-scattered electron
CNO	carbide and/or nitride and/or oxide
DU	depleted uranium (<0.7% U-235, typically 0.2%)
EB	electron beam
EBSD	electron backscatter diffraction
EC	eddy current
EDM	electrical discharge machine
EDS	energy dispersive spectroscopy
HT	hot top
ICP-MS	inductively coupled plasma-mass spectrometry
LANL	Los Alamos National Laboratory
LEU	low-enriched uranium (<20% U-235)
LCP	life cycle plan
LOM	(visible) light optical microscopy
LWR	light water reactor
NDT	non-destructive testing
PFIB	plasma focused ion beam
SE	secondary electron
SEM	scanning electron microscope
SNM	special nuclear material
TEM	transmission electron microscope
TRL	technology readiness level
XRF	x-ray fluorescence
VIM	vacuum induction melt
wppm	weight parts-per-million
wt. %	weight percent
X	generic element
Z	atomic number

1. INTRODUCTION

1.1. Mission relevance, goals and impact

This project was initiated in FY19 in response to the proposal call issued in fall 2017 under the Nuclear Forensics Program the U.S. Department of Energy Office of Nonproliferation Research & Development (NA-22).

This exploratory project examines strategies for encoding unique signatures into uranium at its manufacturing source. The proactive tagging approach enables discriminating forensics information to be extracted should the material be lost and later interdicted. Deliberate upstream tagging at the originating entity for (future) uranium streams provides provenance, while additional, co-located observables in the material can give clues as to the attributes of both pathway and perpetrator, in the sense of revealing any additional processing the material experienced (e.g., bulk melting or welding) before interdiction or recovery of regulatory control.

This project initially set out to explore and extend the possibilities of multiple tagging strategies, including:

1. **Surface Tagging** by inscribing unique patterns on uranium metal surfaces,
2. **Bulk tagging** by altering the bulk chemistry of **metallic forms** of uranium via microalloying, and
3. **Bulk tagging** by altering the bulk chemistry of **uranium dioxide**.

If successful, this work will continue the technical maturation process of these taggant technologies to reach a later point where they could be incorporated into industrial-scale uranium manufacturing and potentially, reprocessing streams as well. It can likewise affect next-generation international agreements.

More broadly, this enables a proactive forensics capability that intentionally controls its circumstances to reshape the playing field to our advantage, with improvements in reliability and robustness anticipated over the longer term. By fingerprinting uranium, it can be known far better than before just where the material originated, which narrows the search to viable suspects, sites, and materials streams while at the same time possibly ruling out the majority of unimplicated entities.

1.2. Overview of FY21 activities and structure of this report

For prior work and a broad survey of tagging strategies that were initially considered, see the FY19 report for this project [2019hac]. Most of the experimental results in the FY20 report [2020hac] are either repeated or updated in this report.

Owing to resource limitations, strategy #3, bulk tagging of uranium dioxide was not pursued beyond initial discussions and a paper study outlining the major issues that was documented in FY20 [2020hac]. The remaining two strategies, surface tagging and bulk tagging (both on uranium metal), were run through to a reasonable completion in these three years, and in spite of the Covid-19 pandemic starting in March 2020, just 6 months after project start.

The following sections cover surface tagging (Section 2) and bulk tagging (Section 3). The conclusions are at the end of these respective sections. An overall perspective and highlights will be further synthesized in a separate final project report soon to follow this one.

2. TASK B. SURFACE TAGGING

2.1. Previous results & discussion

Successful deposition was accomplished via selective laser beam melting in FY20, and follow-on investigations into the persistence of this technique were proposed in [2020hac]. Benchtop characterization using a handheld X-Ray Fluorescence (XRF) system demonstrated detectability of the taggant, and electron microscopy characterization demonstrated that tags were incorporated into the base metal. Unlike laser beam deposition, electron beam deposition was not considered a viable strategy for generating controlled tags [2019hac] when utilizing a lower voltage electron beam system available in Sigma. A reinvestigation of this technique was recommended at the end of FY20 in order to evaluate the newer, higher voltage system available in Sigma, in concert with the foil taggant strategy developed as part of the laser beam deposition technique. A summary of the results obtained in FY19-20 are presented in the following sections, and these results formed the basis for investigation in FY21.

2.1.1 Electron Beam Deposition

Electron beam (EB) deposition was performed in FY19 using Ti-6Al-4V wire on a Ti-6Al-4V base plate; additional deposition details are presented in [2019hac, 2020hac]. Due to the relatively low voltage of the system that was used, as well as limitations on the size of wire, the smallest bead that could be achieved using this technique was a weld bead with a minimum height and width of 0.75 mm and 5.5 mm, respectively. Additionally, the control of the beam deflection was limited; fine details and letters are not possible with this system, and therefore would not be ideal for generating tags with embedded information. In FY19, the newer, high voltage Pro-Beam system was not yet online. The capabilities of the ProBeam system, such as the smaller beam size and faster deflection, were proposed for additional consideration in [2020hac].

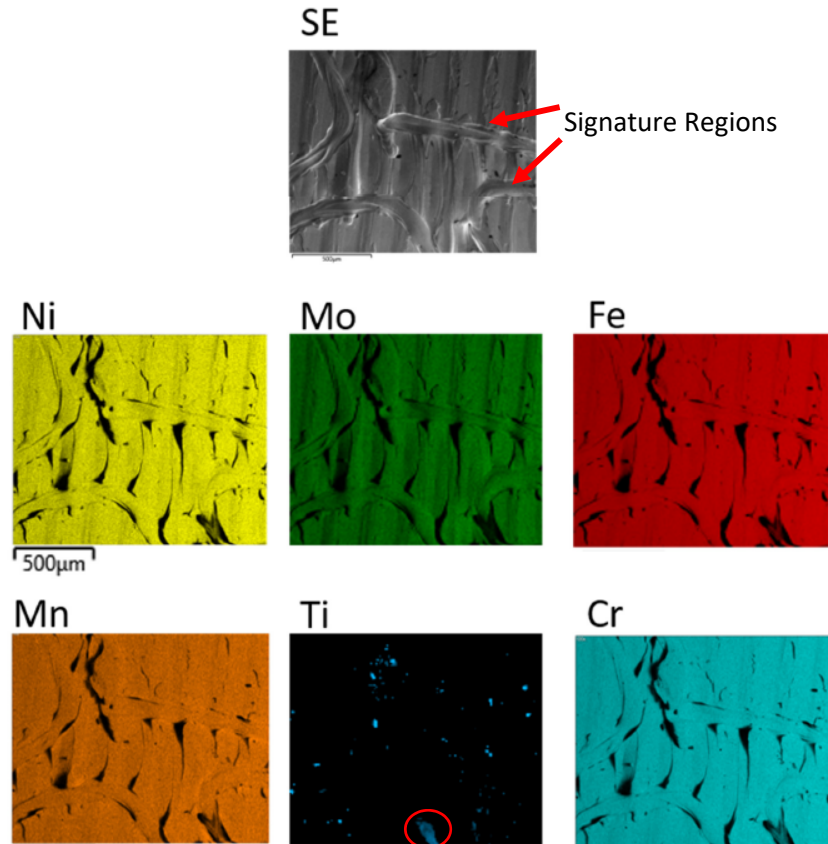
2.1.2. Laser Beam Deposition

Two signatures were generated on the EOS M290 additive manufacturing system through the selective melting of a 0.015 mm pure titanium foil on to a 316L stainless steel plate in FY20; these signatures are shown in Figure 2.1. The resolution of the laser scanning technology allowed for the creation of recognizable “John Hancock” and “Ben Franklin” signatures.



Figure 2.1. FY20 signatures produced with laser selective deposition. The top signature, “John Hancock”, is approximately 4 inches in width. The deposition was produced with Ti foil on a 316L stainless steel plate.

XRF was performed post-test, after the unmelted portions of the titanium foil were removed. The results, recorded three times on the “Ben Franklin” signature, demonstrated measureable titanium from 5.64 to 7.35 wt.% (titanium foil alone would read 100 wt.%). Plan view and cross-section scanning electron microscopy (SEM) was then performed to verify the benchtop results and further characterize the quantity and quality of deposited titanium. Figure 2.2 shows elemental maps from energy dispersive spectroscopy (EDS) in both plan view and in the cross-section of the “John Hancock” signature. On the surface of the deposition (i.e., plan view), titanium is easily detected, but in general, these spots are most likely unmelted titanium that has not been removed prior to characterization. One exception is the very bottom of the titanium map (circled in red) in Figure 2.2(a), where a region of deposited titanium is observed; this deposition aligns with the weld region viewed at the bottom of the secondary electron image shown in Figure 2.2(a), denoted as “SE”. Regions of titanium deposition are further corroborated by examining the cross-sectional view in Figure 2.2(b), where titanium is distributed throughout the melt pool, albeit in relatively low concentrations.



(a)

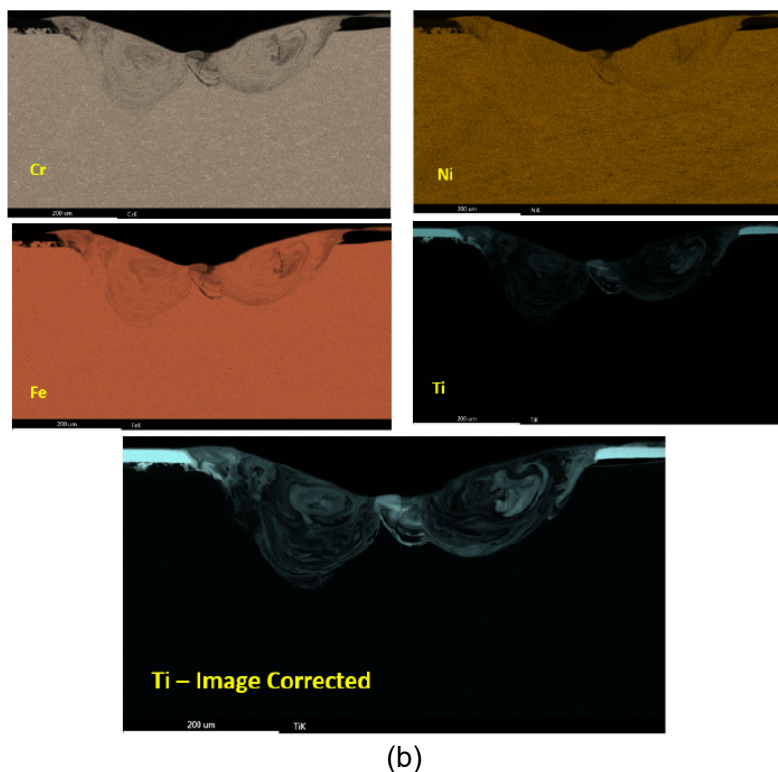


Figure 2.2. EDS elemental maps in (a) plan view and (b) cross-section view of FY20 laser signatures. In (a), the titanium map shows regions of bright blue, thought to be unmelted Ti, with a small region on the bottom center (circled) that shows likely deposition of Ti. The remainder are the elemental maps of expected alloying elements in 316L stainless steel; the EDS maps show consistent results for the base material. In (b), the Ti can be easily observed in the melt pool. The “image corrected” Ti map has a brightness and contrast correction applied to further show the Ti.

The SEM results indicate that it is possible to selectively deposit taggants using laser beam deposition, but these results also demonstrate that the quantity of titanium was variable (i.e., the titanium was not deposited consistently along the weld pattern). In FY21, the effect of laser beam parameters on deposition variability was examined, in order to determine the extent to which deposition could be controlled. Additionally, due to the quantity of unmelted titanium that was available on the surface, the ability to detect a titanium tag after surface defacing was also explored. This defacing would remove both the unmelted titanium and portions (potentially all) of the deposited titanium available for benchtop/field detection, and determine if handheld XRF tools were adequate to capture any remaining, deposited titanium.

It is important to note that all FY20 signatures were produced on 316L stainless steel, whereas FY21 signatures were produced on 304L stainless steel plates. The most significant difference between 304L and 316L is the presence of molybdenum in 316L, added to improve corrosion resistance; this addition is visible in Figure 2.2a. In the context of this project, the difference between the two chemistries of 304L or 316L stainless steels are considered negligible.

2.2. Current Results & Discussion

2.2.1 Review of current (FY21) work

As discussed in Sections 2.2.1 and 2.2.2, electron and laser beam characterization were revisited in FY21. In addition to these items, several other techniques and topics were explored, and are listed below. The list covers items identified in [2020hac], but also several areas for exploration that were identified during the year. Results will be presented in the order listed below.

1. Second attempt at electron beam deposition utilizing two improvements: (1) use of the newer Pro-Beam system, and (2) use of titanium foil as the deposited material.
2. Complete characterization of the original laser signatures, such as electron backscatter diffraction (EBSD).
3. Explore a small scale surface defacing test to determine the persistence of tags.
4. Expand on detection capabilities available within Sigma Division: specifically, Eddy Current (EC) testing was explored as a field-ready non-destructive testing (NDT) technique.
5. Generation of another set of laser beam deposited signatures to evaluate improvements in laser beam parameters.
6. Generate and characterize signatures using the plasma focused ion beam (PFIB) in order to explore the limits on detectability of signatures.
7. Explore the ability to produce a machine-readable tag.
8. Perform a literature review regarding the use of photoluminescence for tagging.

2.2.2. Electron Beam Deposition

The laser beam signatures produced in FY20 demonstrated a resolution that was finer than what could be achieved through wire deposition, and therefore the EB deposition in FY21 explored the use of foil as the deposited material form. Similar to the laser beam deposition, a 0.015 mm thick foil titanium foil was attached to a 304L stainless steel plate using glue on the corners of the foil. The final part is shown in Figure 2.3. The first several attempts were made using the built-in “Pro-Beam” pattern (pre-defined parameters), which was used to demonstrate the ability to produce letters. These attempts were unsuccessful, as the pattern traces an outer rectangle prior to creating the “Pro-Beam” pattern (see boxes in Figure 2.3); this trace is not a weld by definition, as it does not melt the base plate. After the trace, a rectangle is essentially cut from the titanium foil (i.e., not melted/deposited, and becomes a separated, free piece of material not attached to the plate or the rest of the foil) and subsequently lost to the system due to the charged nature of the beam.

The first attempt was used in order to demonstrate built-in features in the system, but the beam parameters were not optimized for deposition. In order to overcome the pattern challenge, a simple circle was attempted next with improved beam parameters in order to generate a weld, rather than a cut. The results were mixed; although the circle pattern appeared to potentially be successful (shown by the circle in Figure 2.3), the inner portion of the titanium foil was still displaced within the system. This presents a challenge to creating an intricate pattern, as the signature will have to be carefully designed to avoid any regions where an enclosed pattern is generated.

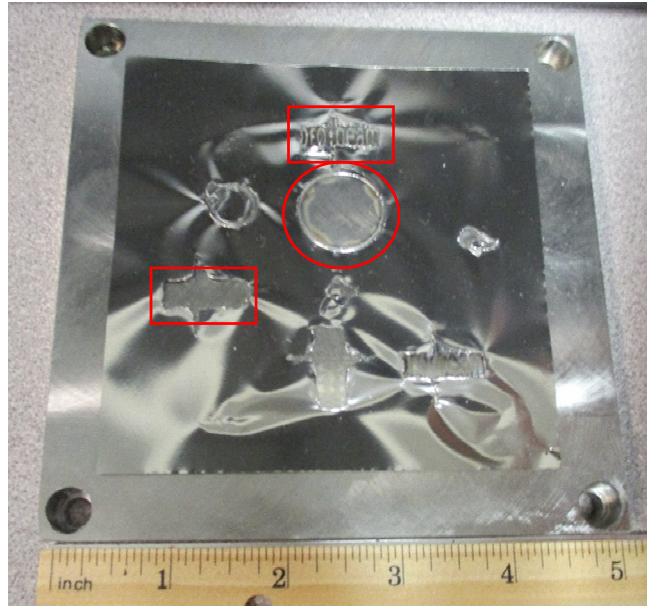


Figure 2.3. EB deposited results, shown in the as-deposited stage. Several attempts at generating a deposited signature are visible. The base plate is 304L stainless steel, and the foil is titanium.

Currently, the use of EB deposition is considered a less desirable option compared to the results observed using laser beam as the energy source. It is possible, though, that EB deposition could be refined further to produce desirable results. For example, if the foil was securely adhered to the base plate along the entire surface area, either via a glue or a welding process such as resistance welding, it may be possible to secure the foil such that it is not lost to the system. In this case, damage to the surface of the substrate, or the introduction of impurities to the signature, would need to be considered. Additionally, as previously discussed, an optimized pattern may be able to create a detailed signature without resulting in unattached foil, but would require effort that is not necessary for laser beam deposition. Due to the additional effort necessary to bring this process to the same success as laser beam deposition, this process is not currently recommended for tagging purposes.

2.2.3. Laser beam deposition

2.2.3.1. Characterization and results from FY20 signatures

The “John Hancock” and “Ben Franklin” signatures produced in FY20 were further evaluated in FY21 to guide the generation of new signatures. EBSD was performed on the cross-section of the signature in order to evaluate the microstructure of the melt pool in a region where titanium was deposited, Figure 2.4. The EBSD results indicate that the grain size is variable throughout the melt pool, including at the deepest points in the pool. Additional conclusions cannot be drawn from the EBSD image shown in Figure 2.4 unless further work is performed to characterize the explicit regions of titanium and stainless steel. Due to the level of effort required with this type of characterization, EBSD is not recommended as a detection technique. EBSD requires a polished surface, specific instrumentation, and a qualified operator. By comparison, EDS and SEM imaging do not require quite the same level of preparation and expertise.

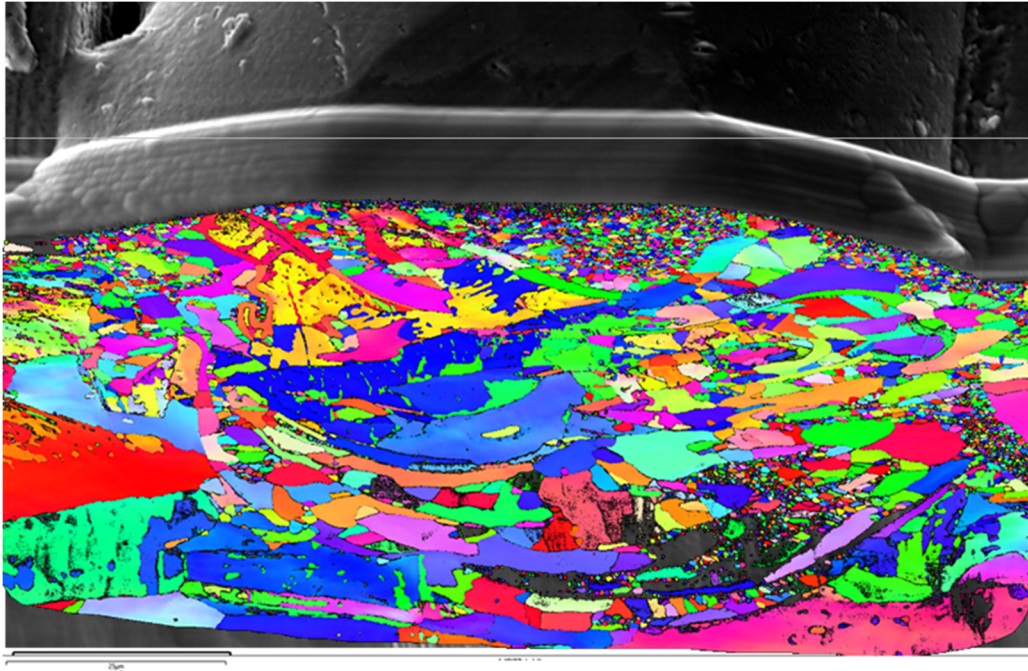


Figure 2.4. EBSD results of a cross-section of an FY20 laser signature. The EBSD results have been overlaid on the SEM image. The gray region on top shows a layer of platinum, which is deposited to protect the signature when the cross-section cut is generated. The colors, added after imaging, demonstrate misorientation between grains.

The EBSD results, especially when compared with the SEM results from FY20, may indicate that the mixing between the titanium and the stainless steel base plate was heterogeneous. One implication of these results is the potential lack of persistency of the tag; if the tag is homogeneous, the entire solidified melt pool will have to be removed in order to prevent detection, but if localized regions of titanium exist, these may be possible to remove without fully removing the weld pool (assuming one can readily locate these signature regions, a difficult task given the relative size). Laser deposited signatures from FY20 were evaluated for this susceptibility by a cosmetic removal (i.e., removal that only erases the visible signature, not the chemical signature) of portions of the signature with 320 grit silicon carbide sandpaper. This exercise was performed by hand. Only half of a signature was removed in order to provide a comparison during Handheld X-Ray fluorescence (XRF) examination. Figure 2.5 shows the comparison of the removed signature to the baseline, intact signature.



Figure 2.5. FY20 “Ben Franklin” laser signature after sandpaper exercise. To the left of the yellow line is the retained portion of the signature, which is used to compare to the portion to the right of the yellow line, which was removed by hand in order to partially erase the visible signature. The entire signature is approximately 35 mm in length.

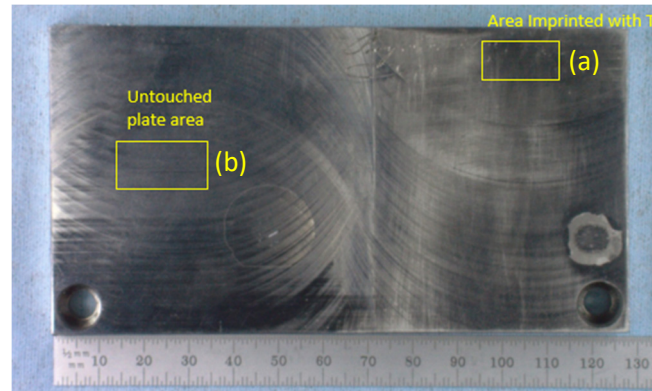
After defacing, XRF revealed that all of the titanium signature had been eliminated (below detection limits of the XRF) during the exercise, while the retained portion of the signature showed a titanium signature that was consistent with the results reported in [2020hac]. Rather than moving towards higher resolution techniques, such as SEM, a second, field-ready NDT capability was explored: eddy current (EC) testing. EC testing is an NDT method that is frequently used to detect cracks and other material changes or defects, such as the effect of heat treatments or corrosion attack. EC is easily implemented in the field, as it does not require bulky instrumentation (i.e., the test unit and probe are considered hand-held) and it is relatively simple for the operator to read and assess results immediately, unlike other tools such as ultrasonic inspection and radiography. Figure 2.6 shows the specific EC test unit and probe that was used for this work.



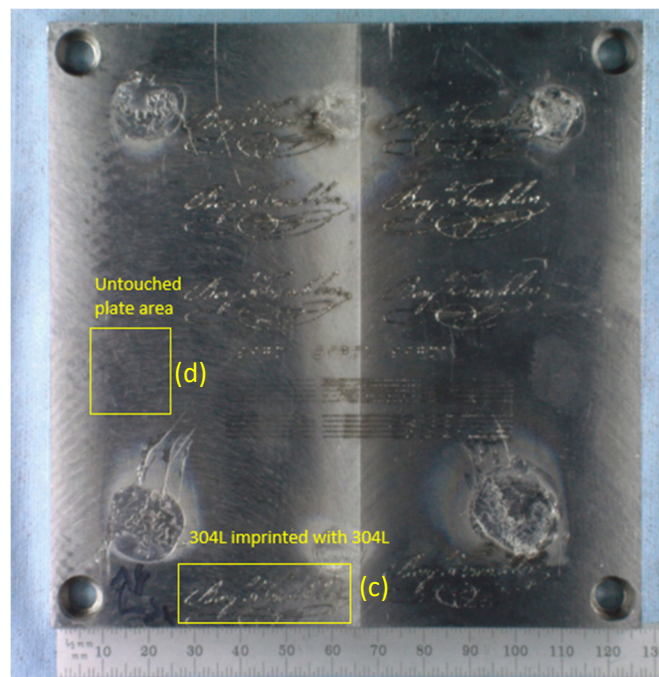
Figure 2.6. Image of Eddy Current unit utilized for this work. The size of the unit, the cost, and the ability to utilize different probes depending on the material shape makes the unit field-capable.

EC was performed on both the “Ben Franklin” signature produced in FY20 as well as a signature created in FY21, discussed in more detail in following sections. In total, four measurements were taken on laser signatures, shown in Figure 2.7:

- One measurement on the sandpaper removed “Ben Franklin” signature from FY20.
- An untouched region of the base plate used in FY20, to provide a baseline.
- A measurement on a “Ben Franklin” signature from FY21, produced without the titanium foil, to determine if the weld alone was enough to generate a measureable signature.
- An untouched region of the base plate used in FY21 as a second baseline, due to the compositional differences between 304L and 316L stainless steel.



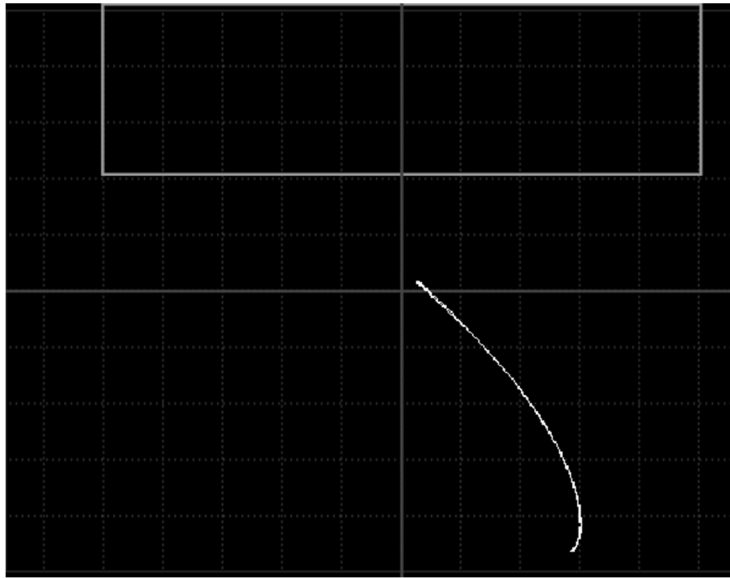
(a)



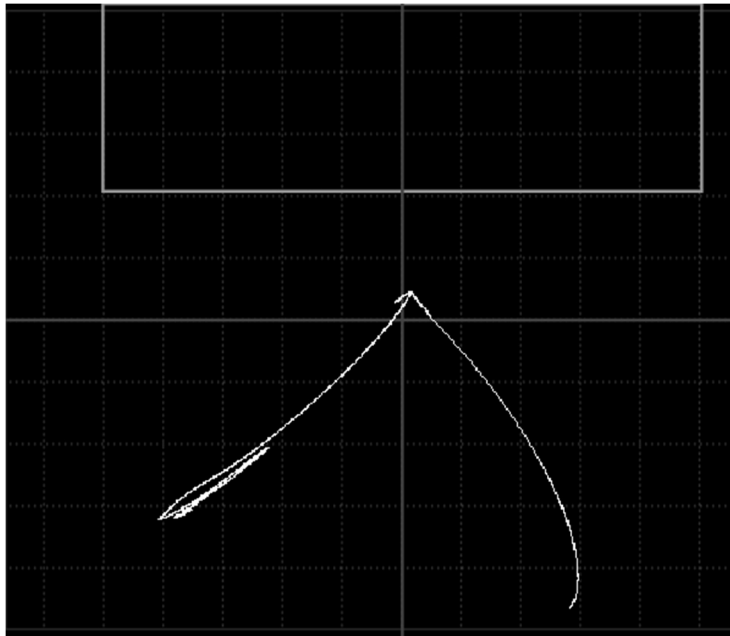
(b)

Figure 2.7. Regions of EC testing of laser signatures. Signatures are from (a) FY20 and (b) FY21. “304L imprinted with 304L” is simply a region of laser deposition where no titanium foil was used.

EC measurements are reported as “lift-off” readings, where the response is measured as impedance plotted as a function of inductive reactance. The measurements on the untouched plate areas, as well as the signature that was generated without a titanium foil, showed identical responses, and matched the shape of the representative response in Figure 2.8 (a). Comparatively, the response from the defaced signature showed a very different shape, shown in Figure 2.8 (b). The difference in the defaced signature response, compared to the other signatures with no titanium, indicates that EC testing is a valid way to detect a chemical variations. Additionally, EC testing utilizes a relatively fine probe, allowing for better spatial resolution in differences compared to XRF. Although the current EC unit does not record data to generate an image of spatial changes, this technology is available, and may allow for the possibility to generate an image of “on” and “off” responses. Finally, other chemical variations (for example, if a foil of a different pure metal or alloy was utilized) would show additional variations in lift-off responses, as would changes in heat treatments, or significant changes to surface, such as cracking. Although this work only demonstrated the response differences between titanium and stainless steel, a large number of permutations are theoretically available for creating signatures. Further work would be necessary to evaluate if the lift-off response differences (from the substrate) are adequate throughout fuel life and in the presence of environmental changes (e.g., CRUD buildup, off-nominal water chemistry variations, etc.).



(a) Lift-off response for untouched plate area in FY20 signature (Figure 2.7a), region (b). This same response was observed for the untouched plate area in the FY21 signature, region (d), and the signature generated without foil, region (c); a total of 3 regions showed this identical response. Therefore, this response is expected for any region measured on a stainless steel base plate (304L and 316L).



(b) Lift-off response for the region where titanium was implanted, and then partially defaced (Figure 2.7a, region (a), and to right of the yellow line in Figure 5). The difference in signal between this response, and the response shown above, is due to the titanium implantation.

Figure 2.8. Lift-off responses from (a) untouched plate area from FY20 signature and (b) defaced signature. The signatures from FY21 that were examined by EC testing both showed similar responses to the lift-off response in (a). Lift-off response is measured as impedance plotted as a function of inductive reactance. The text at the side has further detail.

2.2.3.2 Characterization (using XRF, EC, and EDS) and results from FY21 signatures

Based on the results from laser signatures produced in FY20, several new signatures were generated in FY21; Figure 2.9 shows the layout of the new signatures that were produced in the as-deposited state. For FY21, the focus for generating the new signatures was as follows:

1. Generate “Ben Franklin” signatures while varying laser power and speed, to determine if deposition could be improved. Additionally, signature number 1 was generated by rastering the laser beam twice in the same pattern, to examine if a second pass would improve the deposition.
2. Generate a prototype of a machine readable image, in the form of Braille, which was chosen for ease of readability compared to other machine readable images.
3. Generate baseline signatures with no titanium.

An additional set of laser signatures were generated in order to potentially evaluate statistical characteristics of deposition in the future. These are the straight lines shown towards the middle of the plate, and these lines mimic each of the 6 different parameter sets that were generated for the “Ben Franklin” signatures.

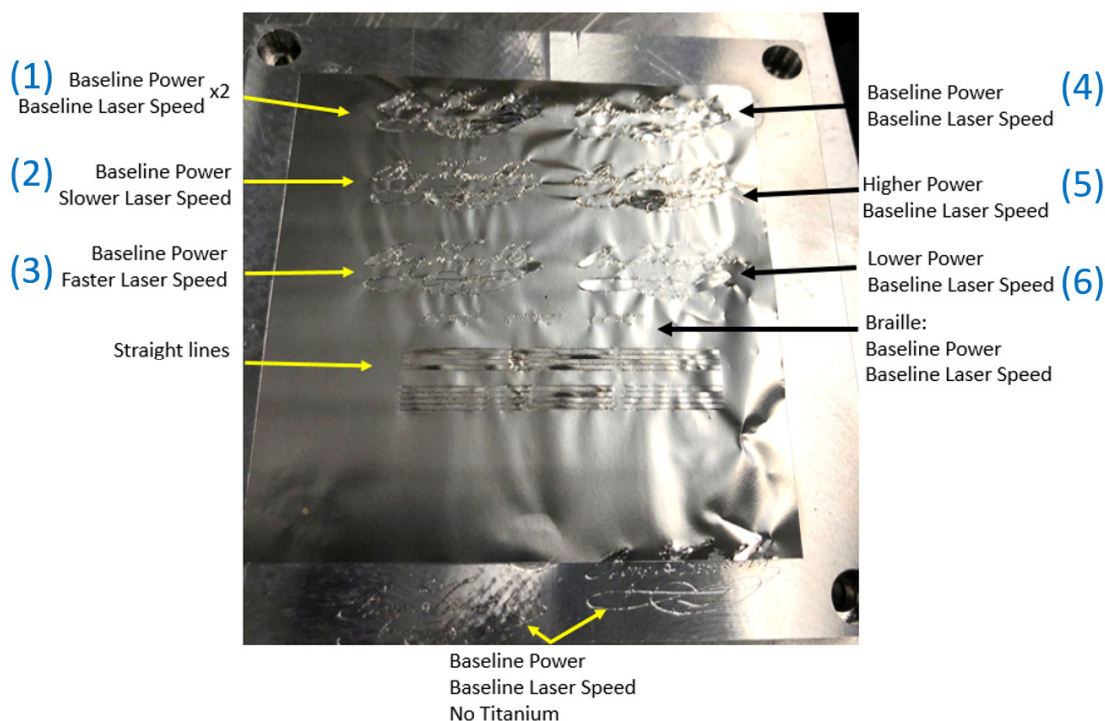


Figure 2.9. FY21 signatures produced with selective laser deposition. Parameters were varied to determine if mixing between the titanium foil and the 304L stainless steel baseplate could be improved. Baseline power and speed are 214 W and 928 mm/s, respectively. Power was adjusted +156 W, -89 W, and speed was adjusted +172 mm/s, -228 mm/s. Blue numbers are for reference.

Prior to destructive characterization, the six “Ben Franklin” signatures were examined using the handheld XRF. The results from the XRF measurements are shown in the Figure 2.10 insets,

after the unmelted titanium had been removed. The XRF results are highly variable, and appear to deviate from the results reported in FY20 for the replicate signature (signature number 4 in Figures 2.9 and 2.10). Specifically, the XRF results of the FY20 signature were between 5.64 and 7.35 wt.%, and the signature deposited in FY21, using the same titanium foil and laser parameters, shows a very small quantity of titanium detected (in some measurements, the XRF did not pick up any titanium). Replication studies should be done if handheld XRF is given more serious consideration, in view of its low resolution and potential operator-to-operator variability.

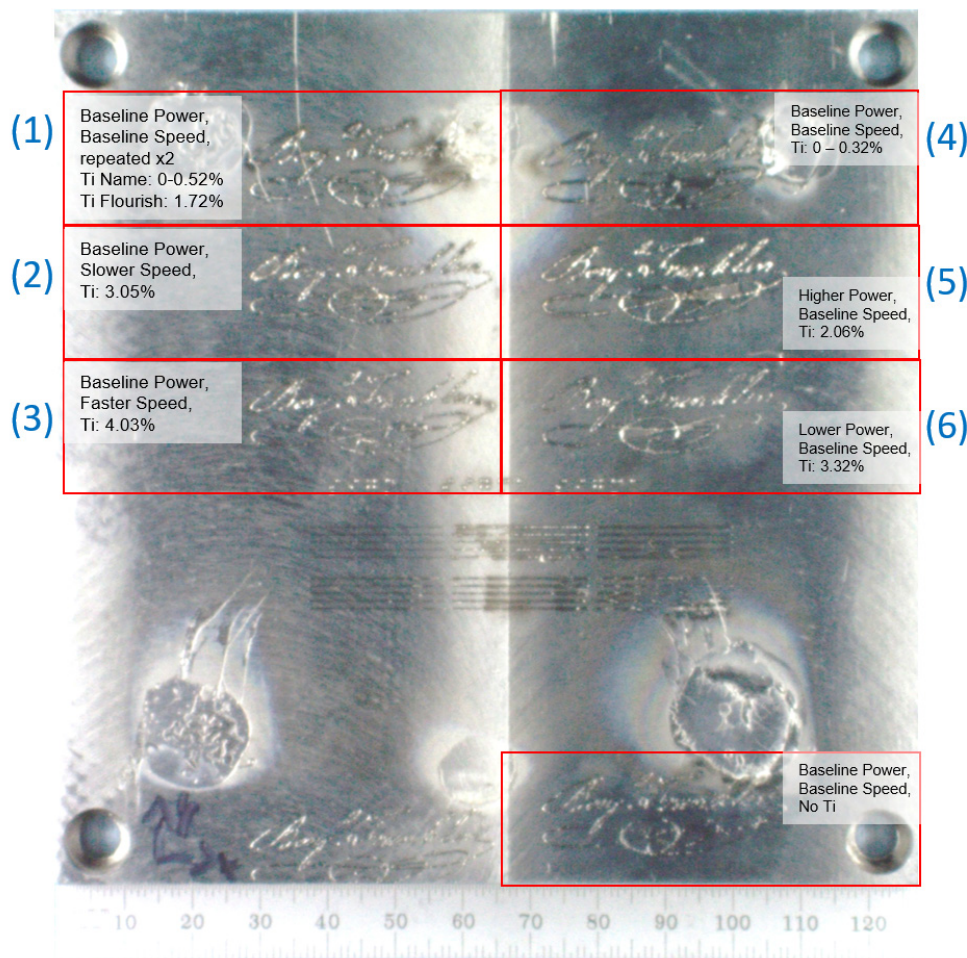


Figure 2.10. Laser signatures and corresponding XRF results (text insets) in wt.%. The left, topmost signature was noted to read different Ti values based on alignment of the XRF: when held over the letters in the signature, very little Ti was observed, but when held over the flourish underneath the signature, Ti was detected. As a control case, the signature at the very bottom of the plate was performed with no Ti foil, and did not show Ti when measured.

In order to separate out variability in the XRF results that could be coming from unmelted titanium that is left behind after the bulk of the foil was removed, SEM images using backscatter electrons were used to discern chemical changes. Figure 2.11 shows an image of each of the six “Ben Franklin” signatures, taken at the same location in order to provide side by side comparison. Arrows show a representation of where the titanium is detected or not detected. In general, although it can be difficult to discern areas of titanium deposition, these areas typically

have small amounts of cracking, and have visible gradients (consistent with the difference in atomic number between titanium and the stainless steel base plate).

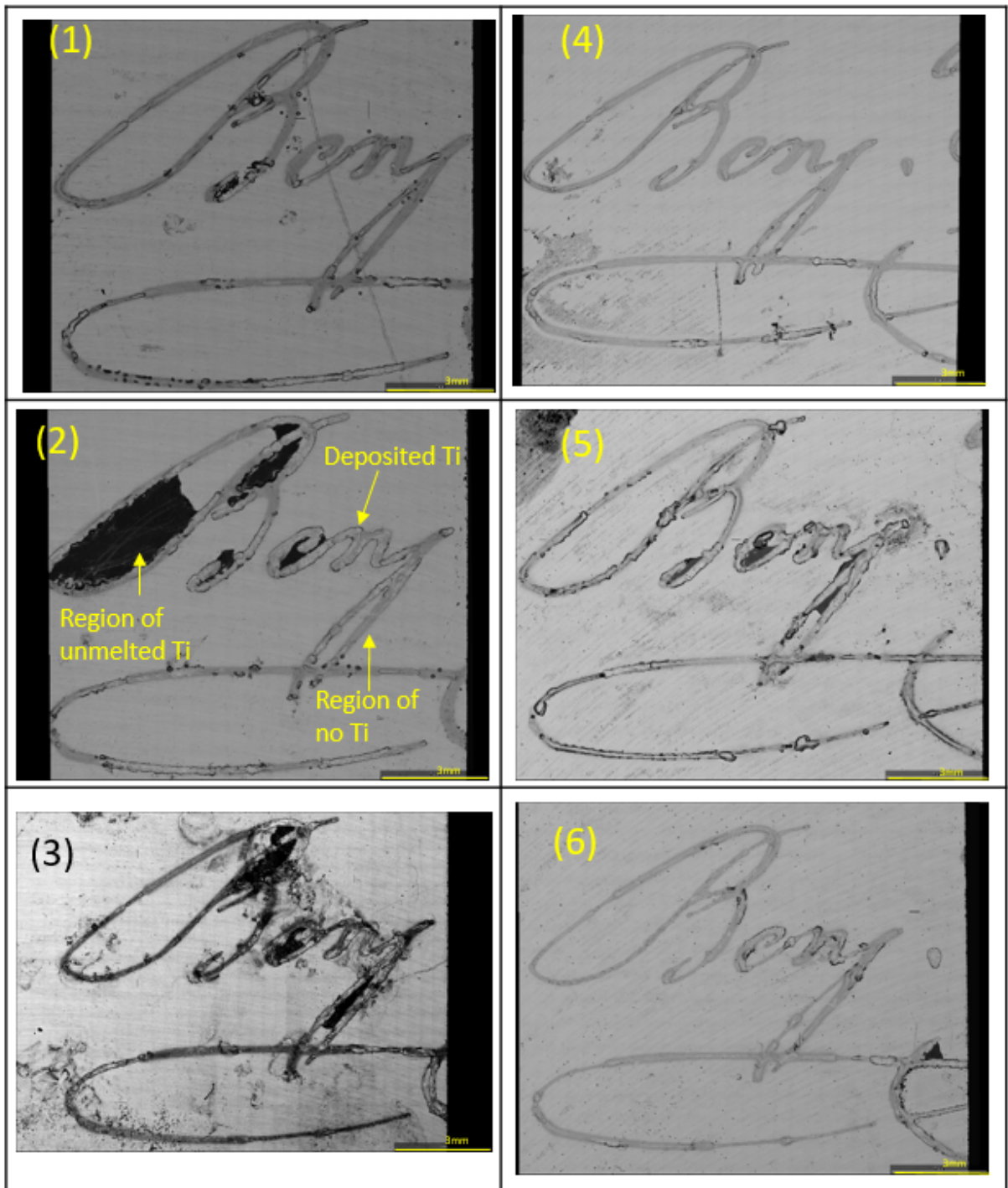


Figure 2.11. Backscatter Electron images of “Ben” signature. Signature 2 is used to demonstrate the appearance of regions with titanium or no titanium.

Comparative EDS images of titanium are shown in Figure 2.12 to better discern differences in titanium deposition, and these images have been adjusted for brightness and contrast. Only a

portion of the “e” from “Ben Franklin” is shown. AztecLive, a rapid-detection software option available with Oxford Instruments EDS detectors, was used for quick detection of titanium in the plan view images shown in Figure 2.11. This tool allowed for quick determination of locations where titanium was present, which are then further evaluated by the user to gather higher resolution images and data. Qualitatively, when using the results shown in Figures 2.11 and 2.12, the laser parameters that show the greatest quantity of deposited titanium are from signatures 2, 3, 5, and 6, though 1 shows a small amount of deposition as well. This aligns well with the handheld XRF results; the unmelted titanium likely biases the titanium concentration artificially high, but even without unmelted titanium (such as in signature 6), XRF can still detect the deposited titanium. The process parameters used in signatures 2 and 5 are likely the best to produce the highest amount of titanium deposition and retain surface quality. The higher power and/or slower speed are both known to increase the amount of melted material, and are consistent with the improvement in deposition.

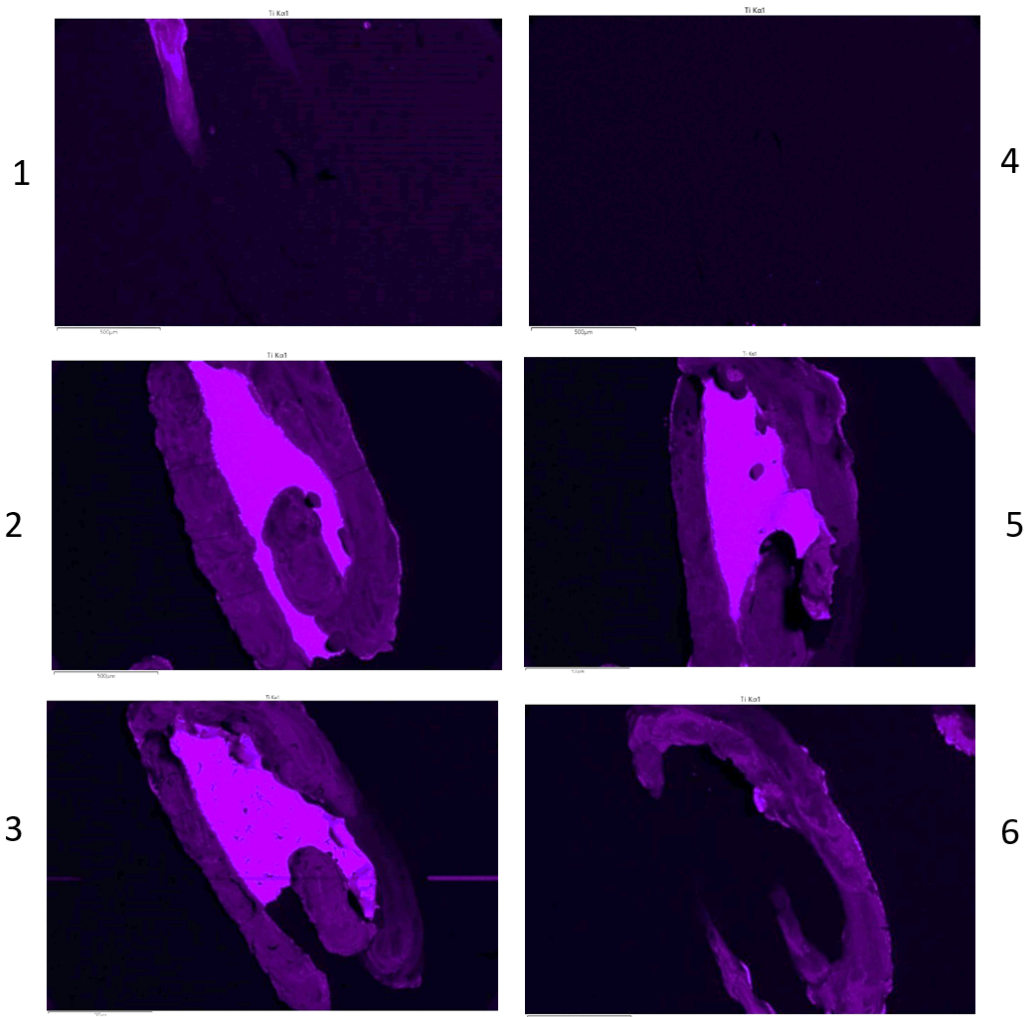


Figure 2.12. Titanium EDS maps taken from the “e” in “Ben Franklin”. Images have been adjusted for brightness and contrast to improve titanium detection, and are rotated compared to Figure 2.11. The bright pink regions in 2, 3, and 5 are from pieces of unmelted titanium foil, whereas the darker pink regions in 1, 2, 3, 5, and 6 are areas of deposited titanium.

Signatures 1 and 4, in contrast to the rest of the samples, show the least amount of deposited titanium. This is especially interesting, given that the laser parameters used for these signatures are identical to those used in FY20. There are several potential explanations for these results. First, the location of the signatures with respect to the margins of the foil may play a role in the quantity and quality of deposition. Signatures 1 and 4 are located towards the upper edge of the foil, and therefore may be affected by a lack of contact between the foil and the plate; the two signatures produced in FY20 were centered within the foil [2020hac]. It is also possible that these signatures exhibit the variability observed in FY20 characterization. Although there may be discrete regions of titanium deposition, these regions are not continuous, appear to be randomly distributed throughout the signature, and therefore are not as easily captured in XRF or EDS compared to parameters that produced continuous distribution of titanium.

The cross-section EDS results also demonstrate an improvement in deposition quality in the FY21 parameter set. Figure 2.13 shows a comparison between the FY20 results using the baseline parameter set and signature 5 from FY21. (FY20 results were used for the baseline parameters – Figure 2.13(a) – rather than signature 4 from FY21, due to the detection of titanium). Both images have been adjusted the same amount to improve brightness and contrast. Qualitatively, increasing the laser power appears to have improved the mixing between the base plate and the titanium foil, promoting a homogeneous distribution of titanium throughout the solidified melt pool.

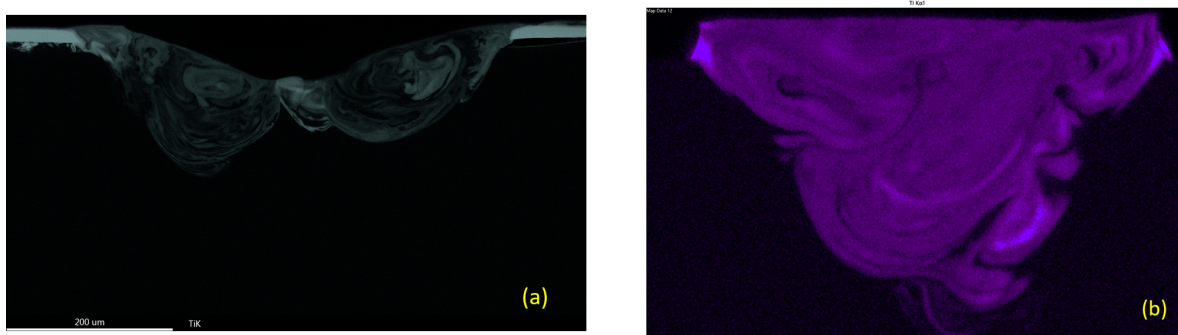


Figure 2.13. EDS results from (a) FY20 baseline parameters compared to (b) FY21 signature 5 (increased laser power). Adjustments have been made to both images to improve brightness and contrast. Note that the (b) FY21 signature is taken at a higher magnification compared to the (a) signature from FY20; the scale bar in (b) reads 100 micron. Although both parameter sets have deposited titanium, the increase in laser power improves the distribution of titanium in the cross-section of the signature as evidenced by increased homogeneity with respect to brightness level in map b.

Due to the size of the Braille results, which are used to represent potential machine readable signatures, no reasonable handheld XRF results could be obtained. Instead, EC testing was used to determine if the dots could generate a signal that was distinguishable from the base plate (i.e., to measure if enough of a deposit was available for measurement), and if each dot was distinguishable from neighboring dots. EC testing demonstrated a clear signal upon the probe passing over each dot that was distinguishable from the base plate. As stated previously,

the current EC system is not such that spatial changes can be captured and stored to produce a two dimensional map, but this technology is available in higher-end EC systems. This exercise proves that a very small, encoded signature (such as Braille, or Morse code) is feasible to produce and detect with field-ready techniques.

2.2.4 PFIB signature results

In order to probe the detection and deposition limits of a surface signature, surface tags were generated using the plasma focused ion beam (PFIB) available in Sigma to deposit layers of platinum in a simple box pattern. For the first signature, approximately 2 μm of platinum was deposited (depth); this pattern is shown in Figure 2.14, both under visible light and using backscatter electrons. After deposition, a handheld XRF was utilized to determine if a field ready instrument could be utilized to detect this signature. Multiple attempts with the XRF yielded no detection of the signature. Additionally, EC testing did not show a distinguishable difference when the probe was passed over the platinum deposit; variations in the signal were noticeable, but it was not clear if this was due to the titanium signature in the vicinity of the platinum deposit or the background noise, as the magnitude of the variations were within the expected noise. A second signature, away from a Ti signature, which deposited a total height of approximately 4 μm of platinum, was also attempted, but this signature also could not be detected with XRF or EC. Since no field-ready detection technique was able to distinguish a PFIB signature, this strategy is not recommended as a stand-alone tag. SEM imaging was able to demonstrate detection, though, as shown in Figure 2.14, so it may be a potential technique to store additional information at the microscopic scale.

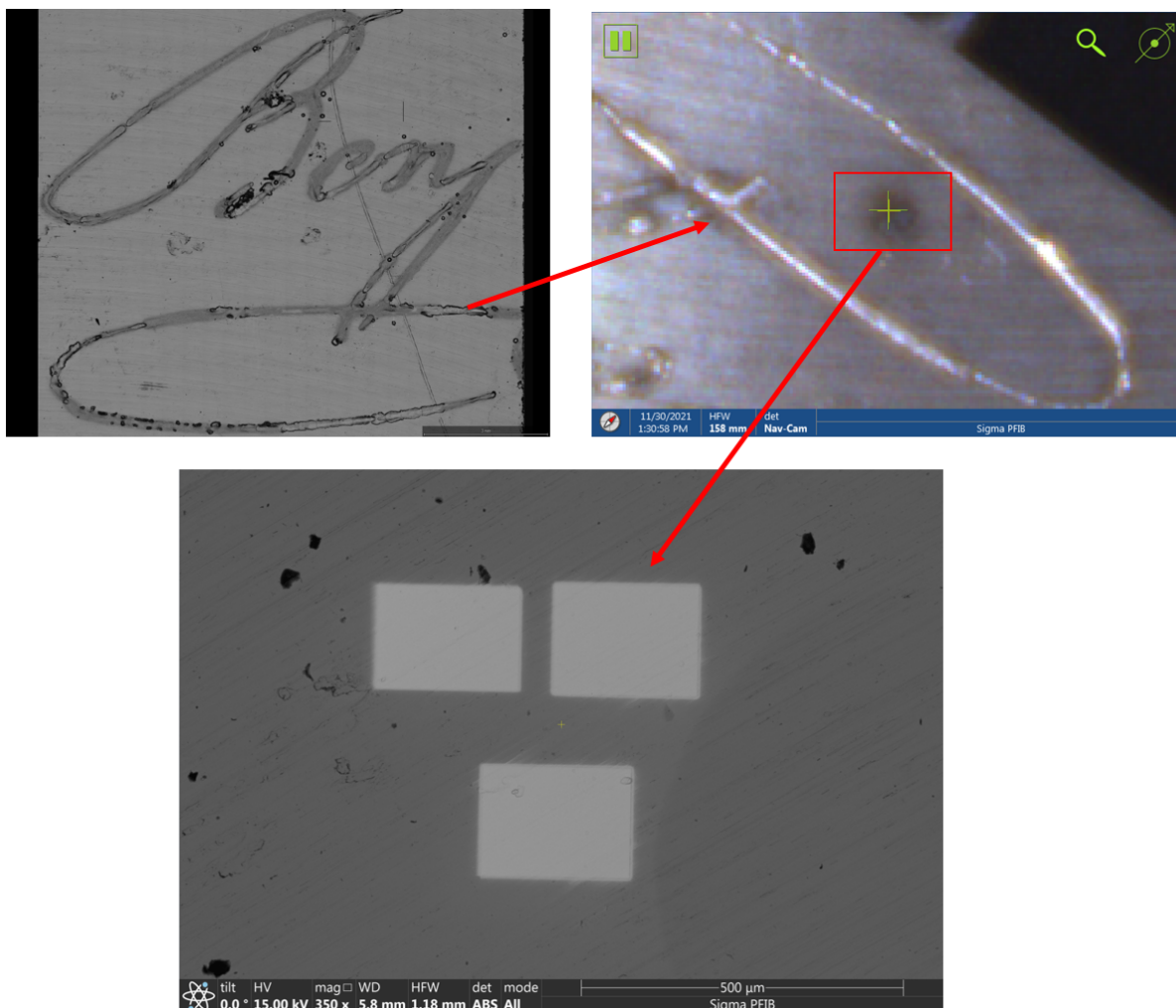


Figure 2.14. Optical (top right) and SEM (top left and bottom) images of PFIB platinum deposit. The platinum was deposited inside of a region where a laser signature had been generated (i.e., the oval in a “Ben Franklin” signature), but was not on top of a laser signature. The SEM image shows the platinum deposit as the lighter box regions, on a stainless steel base plate.

2.2.5. Literature Review of Photoluminescence

Throughout the project, several brainstorming sessions were held in order to determine if other viable options existed for tagging of uranium fuel via bulk or surface tagging.

Photoluminescence was proposed as a potential surface tagging strategy during one of these brainstorming sessions, and a literature review was done in FY21 to determine the feasibility of utilizing luminescent tags for this application. A full report was issued detailing several of the findings from this review [2021blo]. The relevant findings are summarized below:

1. A variety of potential luminescent tags exist for surface tagging applications, including method of generating tag, material type or compound, and maturation of the technology for this application; a summary table is shown in Table 2.1 to provide a qualitative assessment of the various tags available. Although several taggants may be impractical for use directly in a nuclear reactor environment (e.g., using a paint-based tag on a part subjected to flowing water), several strategies were identified as potentially viable candidates for nuclear fuel tagging.
2. Uranium oxide films are known to exhibit luminescent properties, and have been examined as coatings in the form of thin films. The natural luminescence of uranium oxide, and the existence of several distinct wavelengths of luminescence, makes uranium oxide the most likely candidate to generate unique tags on nuclear fuel. It is also possible that all nuclear fuels have some quantity of inherent luminescence; this feature should be explored further prior to attempts to tune or refine uranium oxide as a tag.
3. Plasma electrolytic oxidation (PEO) coatings were identified as a viable candidate for the tagging of zirconium metal; zirconium or zirconium-based alloys are often used as cladding material for ceramic and metallic nuclear fuels. Furthermore, the Sigma facility has the capability to utilize PEO for manufacturing purposes, and therefore future work at LANL to evaluate PEO coatings for tagging cladding is feasible. This underscores the flexibility of luminescent tags, which were identified to be potentially applicable to multiple locations and in multiple forms for nuclear applications, though further testing would be necessary to fully capture this applicability.

It is important to consider luminescent tags as another viable route for the tagging of nuclear fuel, especially in concert with other tagging strategies that have been proposed and explored as part of this project. Utilizing several different tagging strategies provides a robust countermeasure against destruction of tags and counterfeiting, especially when tags can be applied in a variety of ways and may or may not be visible upon first inspection.

Table 2.1. Summary of luminescent tags explored in [2021blo]. All tags/application methods are ranked with respect to applicability as a nuclear fuel taggant.

Attribute of the luminescent tag	Dye	Paint	Thin Films	Thick Films	PEO
Ease of luminophore active ingredient production or attainment	3	2*	3	3	3
Ease of Application	3	3	2*	2	2
Ease of Detection	3	3	3	3	3
Persistence over time (at room temperature conditions)	3	3*	3	3	3
Persistence in a nuclear reactor environment (radiation, 300°C H ₂ O)	1	2*	3*	2*	2*
Compatibility with Metallic Uranium Fuel (e.g. LEU-10Mo)	1	2*	3	2*	1
Compatibility with Oxide Uranium Fuel (UO ₂)	1	2*	2*	2*	1
Compatibility with Cladding (e.g. Zircaloy)	2	3	3	3	3
Compatibility with Other Metals	2	3	3	3	2
Compatibility with Other Materials	3	3	2*	2*	1
Ability to Conceal Tag	3	3	2	1	1
Multifunctionality (corrosion detection, protective, scannable, etc.)	3	3	2	3	3
Ability to Produce Fine Detail	3	3	3	2*	2*
Permutations Available	3	3	3	3	3

*=more research is necessary, the choice of luminescent compound greatly affects this, or prohibitively expensive.

Stoplight Chart Legend	
1	This is not possible or compatible, or there is no work on this subject.
2	With additional research or development, this may be possible, or there is a lot of variability in the results.
3	This is something that has been done or studied before, is very likely to succeed, or is compatible fuel or cladding.

2.3. Surface tagging conclusions

The results in FY21 confirmed the variation in titanium detection in surface tags that was observed in FY20. While variation is still observed in the FY21 tags, improvements to detection and overall quality of the tag were produced through either slowing the speed or increasing the power of the laser during selective laser deposition. Additional optimization of the laser beam parameters is likely possible, but several of the signatures produced in FY21 demonstrate adequate quality to be detected with techniques such as XRF, EDS, or SEM.

In addition to improving surface tagging quality, improvements were also made in the areas of detection capabilities and understanding persistence of the surface tags. EC testing has demonstrated to be a field-ready technique that is capable of detecting titanium deposits that are no longer traceable visually or with XRF. Furthermore, EC testing is likely the only field-ready technique evaluated in this project that is capable of detecting and capturing the spatial resolution of a machine readable code. This spatial resolution was not shown in this project, due to the limitations of the EC unit that was procured, but other EC systems are available for purchase that would have these capabilities. Although this technique does require contact between the part/material and the probe, the ease of use, technology maturation, and resolution of the instrument and probe make this technique a viable option for detection of a variety of surface tags (such as chemical tags, cracking/surface features, etc.).

Finally, EB deposition was confirmed to be a less successful surface tagging tool when compared to laser beam deposition, and therefore taken off the table for further exploration in this project. At the same time, several new methods, in the form of photoluminescent tags, were identified. The use of a luminescent tag, especially in concert with other tagging techniques, shows promise and warrants future research for use in or on nuclear fuels depending on the needs and limitations of the end user, especially when considering the inherent luminescence of uranium oxide. This type of tagging would potentially allow for surface and bulk tagging without the introduction of further alloying elements or impurities. Additionally, PEO coatings were also identified as a potential method to tag the cladding. Although the technical readiness for this tagging technique is considered low with respect to surface tagging of fuel, the literature review presented in Reference [2021blo] demonstrates that viable options may exist.

A summary table of the surface tagging and detection techniques is given in Table 2.2.

Table 2.2. Summary of surface tagging and detection strategies evaluated as part of this project. Relative success is shown for each item. Red indicates an item that was determined to be not successful, is not viable, or is not a path worth considering when compared to other options. Yellow indicates an item that is feasible, but additional work is necessary to prove success for surface tagging. Green indicates an item that demonstrated initial success as part of this project, and is the most promising candidate for further exploration.

	Surface Tag or Detection Method		Summary
Deposition Technique	Electron Beam Deposition with Wire	Red	Utilizing an older EB system, the wire deposition was too large for surface applications, and limited in potential designs (i.e., only a straight line was possible). This is due to the wire size and low voltage of the system.
	Laser Beam Deposition with Ti Foil	Green	Utilizing an additive manufacturing system (EOS M290), selective laser deposition was able to create intricate Ti-deposited signatures (John Hancock and Ben Franklin replicas) on SS 304L and 316L base plates.
	Electron Beam Deposition with Ti Foil	Yellow	Utilizing a newer EB system and titanium foil (rather than wire), signatures were attempted in similar detail to the laser deposition. Titanium deposition was not successful, primarily due to the charged nature of the electron beam. Further exploration into securing the foil to the base plate may show success, but was not attempted due to success with laser beam deposition.
	Laser Beam Deposition with Ti Foil, Improved Beam Parameters	Green	Improvements on the successes using laser beam depositions from FY19 and 20 were attempted in FY21. Slowing the laser beam speed, and/or increasing the power of the beam, showed improvements in deposition by way of an increase in deposited titanium across the length of the signature, and homogeneity in the solidified melt pool between the titanium and the stainless steel base plate.
	Plasma Focused Ion Beam	Red	Attempts at depositing very small signatures using platinum were not successful; deposition was not detected using X-ray fluorescence (XRF) or eddy current.
Detection Technique	Electron Microscopy: BSE, EDS	Green	Imaging using backscatter electrons (BSE) and energy dispersive X-ray spectroscopy (EDS) was successfully used to detect titanium in the plan and cross-section views. Improvements in laser beam deposition made detection in the plan view easier in FY21 compared to FY20. These techniques do require a scanning electron microscope, but are easy for a trained user.
	Electron Microscopy: EBSD	Red	Electron backscatter diffraction (EBSD), although useful for grain size investigation, was not pertinent to this project as a standalone microscopy tool, and requires additional skill and training for an operator to generate.
	XRF	Yellow	XRF was utilized as a field-ready technique to determine the presence and quantity of titanium in a signature. Although useful for detecting titanium quickly, results showed bias due to remnant (unmelted) titanium that was left behind after deposition, and there was no feasible way to detect a spatially varying signature, as the measurement is taken from a large surface area.
	Eddy Current	Green	Eddy current showed significant success in detection of titanium, even after the signature had been partially removed by hand via sandpaper. Although not demonstrated due to the eddy current system available, spatial detection of titanium (i.e., detection of a pattern) is possible with available eddy current systems on the market.
	Photo-luminescence	Yellow	A literature review [2021blo] showed a variety of potential luminescent tags exist. Although some are likely impractical for use in a nuclear reactor environment, due to environmental degradation of the tag, compatibility with the fuel, degradation of reactor performance, etc., several strategies were identified as potentially viable candidates for nuclear fuel tagging.

3. TASK C. BULK URANIUM METAL TAGGING

3.1. Summary of technical approach

This task focuses on **chemical tagging** – adding natural isotopes of various elements in specific ratios to provide a unique taggant signature in bulk metal uranium. Ideally, the ratios of the taggant elements will remain the same even with dilution through further material processing. This strategy is detectable through bulk chemical analysis such as inductively coupled plasma-mass spectroscopy (ICP-MS). A different strategy – **second-phase tagging** – also arises since the formation of second phases is likely to occur when alloying elements are added to a metal. To detect these other phases, scanning electron microscopy (SEM) and energy-dispersive X-ray spectroscopy (EDS) are necessary. Other effects brought on by minor alloying may be measurable (e.g. slight shifts in reaction temperatures), but the indirect or indicator-only identification methods and signatures are left as potential future work. Based on previous work, the alloying elements are likely to segregate into four general phases: 1) intermetallics, 2) rare earth oxides, 3) carbide, nitride, and/or oxides, or 4) incorporate into common UC inclusions [2013hac]. In summary, by adding various alloying elements to bulk uranium, two tagging strategies are possible: a specific ratio of elements and second phase segregation.

The potential taggants were probed for detectability and behavior in three distinct stages of experimentation. The elemental additions were first alloyed with uranium at relatively high concentration levels (0.5 wt.%) in unique groupings of four elements in order to probe initial detectability. These are referred to as baseline castings, and have about 98 wt.% uranium by difference. Further mixing and dilution castings were performed in order to observe both species interaction as well as detectability under more dilute conditions. Finally, a recycling study was used in order to determine the persistence of the alloying additions after repeated melting and casting of the same material. A variety of microscopy and chemical assessment techniques were utilized to track the fate of the taggant element additions.

3.2. Activity overview

3.2.1. Casting and sampling

All materials were made using depleted uranium (DU) metal. The nominal carbon level was 245 wppm; total other impurities 750 wppm maximum. Vacuum induction melting (VIM) is a common technique used to cast uranium with a standard industrial manufacturing process. Once material has been cleaned, sampled, and weighed, it is loaded into a graphite crucible that sits on top of a graphite mold. The locations where graphite will contact metal is coated in yttria to limit carbon uptake in the metal during casting. The crucible and mold sit atop a graphite pedestal, to place the mold at the correct height within the hot zone of the furnace. The crucible, mold, and pedestal are instrumented with thermocouples to record the thermal profile during casting. The final setup step is the addition of insulation, including graphite felt and graphite foam.

All 18 of the castings in this study utilized a single coil VIM furnace to cast plates of uranium alloys. The metal melts in the crucible while the mold is heated to a specified thermal profile under vacuum conditions. When the goal temperatures are achieved, a stopper rod (also yttria coated graphite) is raised to allow the molten metal to flow into the mold. With unalloyed

uranium, the goal temperatures at time of pour are at least 850°C at the bottom of the mold, at least 1130°C at the top of the mold, and the molten metal at approximately 1300°C.

Table 3.1 lists all 18 alloys produced throughout this 3-year study. The baseline alloys (~16 kg) were the first four plates produced. One of the baseline alloys, 19C1-016, reacted with the crucible during VIM casting and was only analyzed for chemistry. The other three successful baseline alloys were combined with one another to produce three mixed alloys while one of them was combined with unalloyed DU to produce the one dilution alloy (all ~5 kg). Finally, the three successful baseline alloys were combined to produce the alloy that was used throughout the recycling study, whose casting mass ranged from 17 kg (1st melt) to 12 kg (final, 10th melt).

Table 3.1. An overview of the 18 uranium alloy castings processed throughout this study.

Group	Casting ID	Taggant Elements Included
Baseline alloys	19C1-010	Ti, Mn, Tb, Au
	19C1-014	Al, Sc, V, Pd
	19C1-015	Co, Nb, W, Ir
	19C1-016*	Ni, Ge, Ce, Ta
Mixed alloys	20C1-076	Al, Sc, V, Co, Nb, Pd, W, Ir
	20C1-077	Al, Sc, Ti, V, Mn, Pd, Tb, Au
	20C1-078	Ti, Mn, Co, Nb, W, Ir, Au
Dilution alloy	20C1-080	Co, Nb, W, Ir
Recycling study	21C1-105	Al, Sc, Ti, V, Mn, Co, Nb, Pd, Tb, W, Ir, Au
	21C1-107	
	21C1-109	
	21C1-111	
	21C1-112	
	21C1-113	
	21C1-114	
	21C1-115	
	21C1-116	
	21C1-118	

*19C1-016 reacted in the crucible; results from this alloy are questionable. Due to resource limitations, it was not studied or used further.

Once the casting has been removed from the mold, chemical analysis and microscopy samples are taken from the as-cast part. For chemistry analysis, samples consisting of ~0.25-inch drilled chips (sometimes referred to as “pigtailed” or turnings) were taken from various locations along the height of the plate. All drilled chips were removed on a manual mill without coolant or cutting fluid using a ¼” diameter bit and a slow spindle speed to prevent sparking or rapid oxidation, which would spoil the sample. Metallography samples were cut on a bandsaw or with a wire-cut electrical discharge machine (EDM).

3.2.2. Bulk chemical analysis

The taggant elements in all 18 castings were measured via inductively coupled plasma-mass spectroscopy (ICP-MS) at two different LANL laboratories. The first step when performing ICP-MS is to digest the sample via acid. The digestion is visually assessed to make sure the whole sample was fully dissolved. The ICP-MS method turns the dissolved sample into an aerosol, which is then introduced to the plasma torch. The resulting ions are entrained in the plasma gas and measured by a mass spectrometer. Assessing the differences between the techniques used at the two labs is part of a separate study being performed by participants in a NA-22 Venture project.

Carbon analysis was performed using a LECO CS844 carbon/sulfur analyzer. A combination of an induction furnace, high oxygen atmosphere, and an accelerator material results in combustion of the metal chip samples. Any carbon within the sample is released to combine with oxygen. The gas is detected by a pair of non-dispersive infrared cells and output to the user as wt% carbon.

3.2.3. Microscopy

Various samples from the baseline alloys and mixed/dilution alloys were metallographically mounted, polished, and examined via light optical microscopy (LOM) and scanning electron microscopy (SEM). Two different SEMs were utilized: an Inspect SEM and a Helios G4 UXE Plasma FIB/SEM. Representative inclusions were analyzed by energy dispersive X-ray spectroscopy (EDS) to determine chemical makeup. EDS has a spatial resolution of about 1-2 microns. When inclusions are smaller than 1-2 microns, part of the EDS spectra will be from the surrounding matrix, which originates to the side and/or underneath the particle of interest. Also, peak overlap can cause detection issues if not accounted for. When performing EDS on uranium, there are several confounding issues with carbon detection. Carbon is difficult to detect via EDS since it is pervasive in vacuum systems and deposits onto a surface under an electron beam and light elements tend to be difficult to detect more generally. Also, the relatively low-energy characteristic X-rays emitted from carbon are absorbed by the uranium matrix. These issues combine to cause pure uranium to show the same amount of carbon via EDS as a uranium carbide inclusion. Due to all of these concerns, the EDS results presented in this study are qualitative only, and the order of elements listed on the various micrographs throughout the report are arbitrary.

3.3. Review of prior (FY19, FY20) work

3.3.1. Baseline alloys: design and procedure

To begin the design of the alloys, the taggant elements were determined. A thorough explanation can be found in the FY19 report [2019hac]. To summarize, four different filters were applied to the periodic table leading to a final selection of 16 elements: Al, Sc, Ti, V, Mn, Co, Ni, Ge, Nb, Pd, Ce, Tb, Ta, W, Ir, and Au. These raw alloying elements were weighed into individual sets and co-melted in the inert atmosphere of a non-consumable arc melter. This resulted in four master alloy buttons with four alloying elements per button at a balance of ~85 wt% U per button. Those four buttons were then down blended with DU to form four baseline alloys (one button per casting) with each alloying element at the ~0.5 wt% level and a balance of ~98 wt% U per alloy. The castings were processed using a VIM furnace resulting in four baseline alloys. More details can be found in the FY19 report [2019hac].

The plates were then sectioned for metallography and machine turnings were taken for chemical analysis. This process is illustrated in **Figure 3.1**. The process should result in a simple taggant ratio of 1:1:1:1 for each baseline alloy. Each alloying element can also be predicted to segregate into a specific second phase, summarized in **Table 3.2**. Intermetallic phases consist of two or more metals, and do not need to contain uranium. In many instances, the metals in carbide, nitride, and/or oxide formers can substitute for each other in the metal sublattice. C, N, and O might also substitute for each other on their interstitial sublattice, through this is of somewhat less importance for this project. V, not a strong carbide former on its own, is expected to simply incorporate into UC. More details can be found in the previous report where ternary and higher order phase diagram interactions were neglected (e.g. U-Al-Ti) and are not well known in most cases [2019hac]. Also note the results presented here are from as-cast material. Wrought and/or heat treated products will look different, mainly in the microscopy; apart from potentially higher levels of H and O, the chemical analysis would remain unchanged.

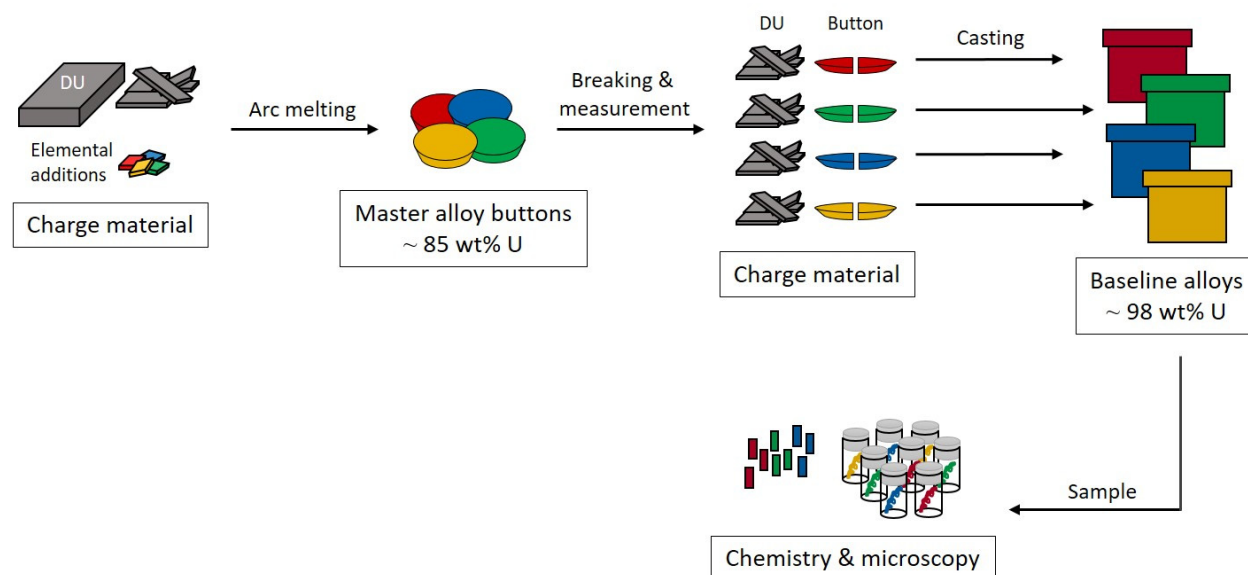


Figure 3.1. Schematic of the processing of the baseline alloys.

Table 3.2. Predicted second-phase segregation for the chosen taggant elements.

Taggant Element	Predicted Second Phase
Al, Mn, Co, Ni, Ge, Pd, W, Au	Intermetallic
Sc, Ce, Tb	Rare-earth oxide
Ti, Nb, Ta, W	Carbide, nitride, and/or oxide
V	Incorporate into uranium carbide (UC)

3.3.2. Baseline alloys: chemistry results

Bulk chemical analysis was performed via ICP-MS while carbon analysis was performed using a LECO CS844 carbon/sulfur analyzer. Chemistry analysis from each baseline casting is shown in the FY20 report [2020hac]. None of the castings showed any significant chemistry differences between the two locations that were sampled in each casting. Only three of the alloying elements, V, Co, and Ir, measured close to their calculated values. Nickel also measured at the anticipated level, but the results are questionable since the master alloy reacted with the crucible during casting. The low measured chemistry results are likely the result of poor mixing in the master alloy button and/or the VIM furnace casting. However, the low measurements are not a showstopper, and adding the elements in specific ratios is still a possible tagging strategy even in light of these results.

Note that “calculated values” for the mix, dilution and recycle #1 alloys are based on charge masses and Lab A chemical analyses, which were only done on the intentional tagging additions, not impurities or cross-contamination (e.g., Al, Sc, Tb – all detected in SEM, and possibly W, which was not seen by SEM but had high readings in chemical analysis). Analyses from Lab B included all 16 elements (plus Cu, possible pick-up from the arc melter hearth and Y, possible from the Y_2O_3 mold coating) whether intended as a taggant or not; however these data were not rolled into the calculated value. This remains for ongoing work as part of the Venture to get statistically significant chemical analyses. At a minimum this more complete accounting would especially explain the discrepancies in the Al chemical analysis results.

3.3.3. Baseline alloys: microscopy results

Microstructural analysis was performed using light optical microscopy (LOM), scanning electron microscopy (SEM), and energy-dispersive X-ray spectroscopy (EDS). In FY20, one baseline casting was analyzed, 19C1-010. The four elements purposely added to this alloy were Ti, Mn, Tb, and Au. Based on the LOM images, there was no significant difference in the microstructure along the height of the plate, including the hot top. Based on SEM and EDS, the four alloying elements did segregate to the predicted phases, and representative images are shown in

Figure 3.2. Various intermetallics containing Mn and Au were found throughout the plate. The local chemistry of those phases did vary along the height of the casting. Terbium oxide was found in the middle and the hot top. Titanium carbide particles were found throughout the plate. The faceted morphology of those particles is similar to U(CNO) particles that are commonly found in unalloyed uranium metal. Distinguishing the various X(CNO) particles, which often manifest with similar geometries, requires BSE or EDS, which could make them an interesting second phase taggant. However, because TiC has a high melting temperature and low density relatively to liquid uranium, these particles could be relatively easy to remove via flotation during casting, though results from this study find that at least in certain alloying ranges, this may not be an issue.

Al and Sc were not deliberate additions but were detected by SEM in various particles, often along with the intentional tagging elements. This presumably arose from cross-contamination during the synthesis of the master alloy buttons. Chemical analysis of 19C1-010 (Appendix) showed a high level of Al, about 800 wppm but a more modest level of Sc, about 12 wppm.

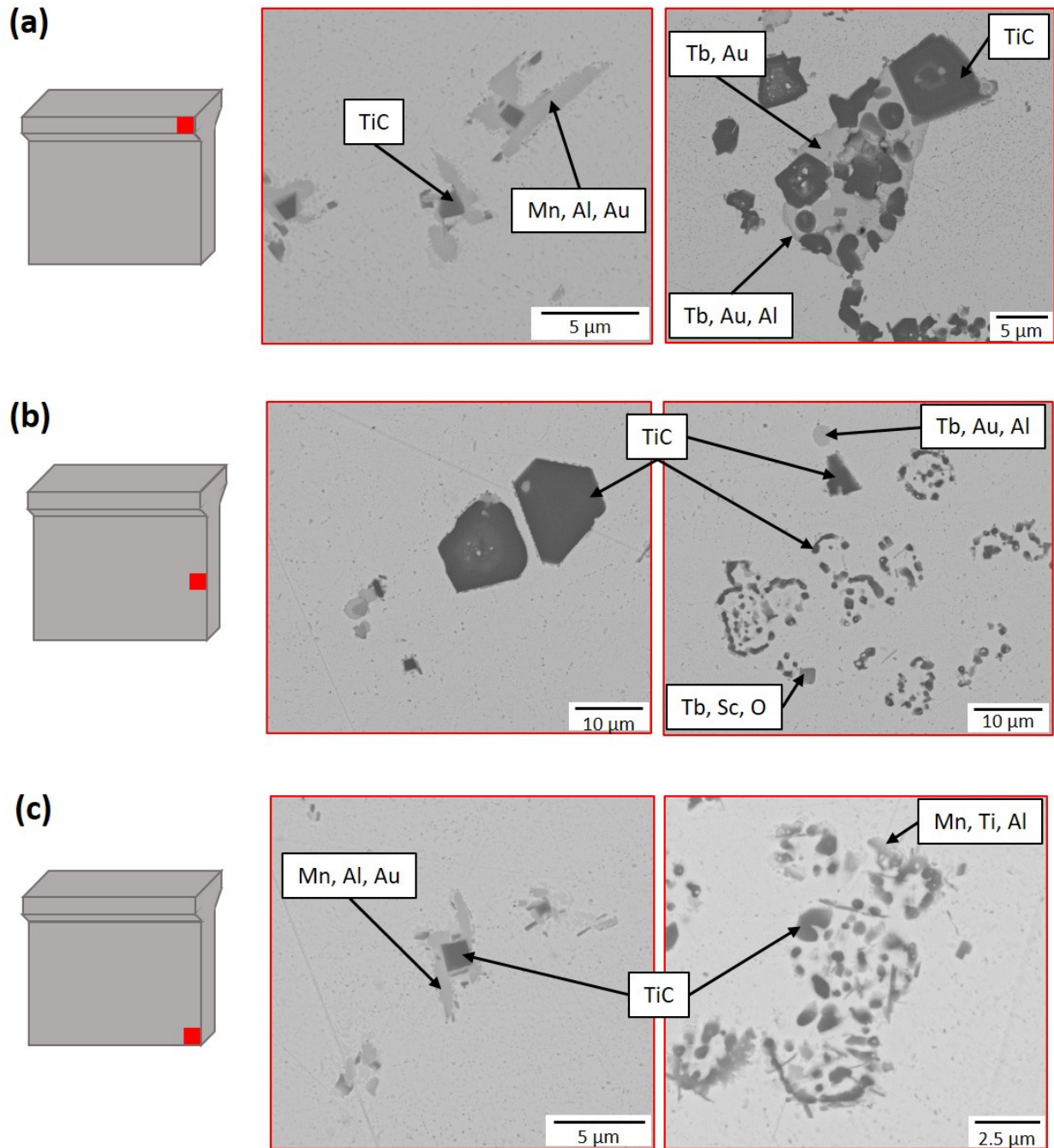


Figure 3.2: Representative BSE-SEM images taken from the (a) hot top, (b) middle, and (c) bottom of 19C1-010. All three areas show faceted TiC particles along with globular intermetallics of varying chemistries. Al and Sc were observed but not intentionally added, suggesting cross-contamination during master alloy manufacture.

3.4. FY21 activity – baseline alloys

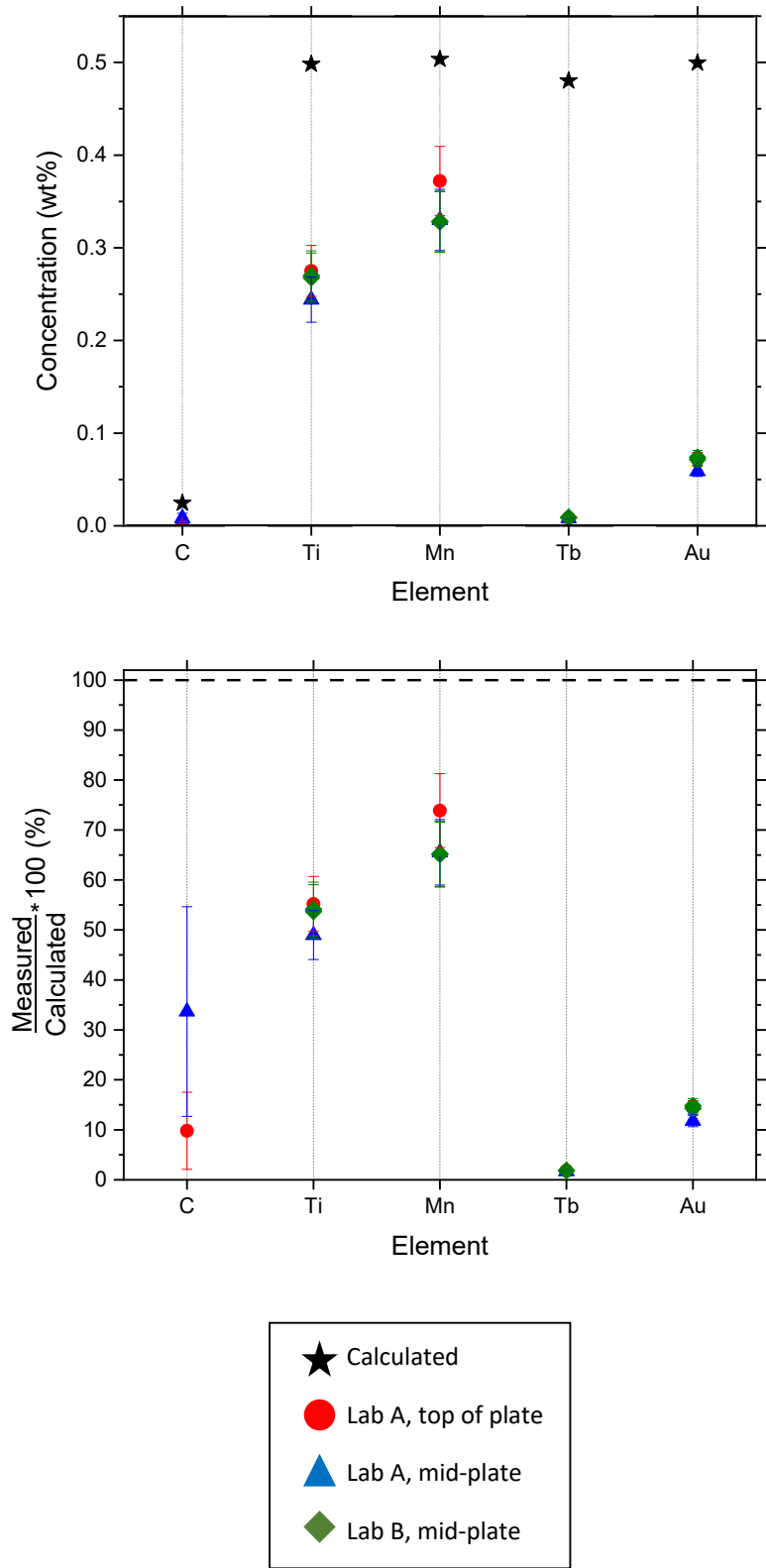
3.4.1. Addition of elements in specific ratios – chemistry results

When it comes to the addition of elements in specific ratios, two things are important: manufacturability and detectability. Manufacturability encompasses incorporation of the element into the bulk uranium and segregation of the element within the casting while detectability concerns whether or not the element can be measured while. In order to better access detectability, two laboratories at LANL performed bulk chemical analysis via ICP-MS to compare to previous results. These two labs will be referred to as Lab A and Lab B throughout the remainder of this document. The results reported in FY19 were from Lab A. Carbon content was also measured for each alloy using a LECO CS844 carbon/sulfur analyzer. Carbon was not intentionally added, but it does play an important role in second phase formation due to its ubiquity as a common impurity in uranium and uranium alloys. For the baseline alloys, a carbon content of 245 wppm was assumed, which is middle of the road as far as uranium goes. 19C1-010 values measured low, which tends to occur with Ti present. 19C1-016 measured high, which was expected due to the reaction in the crucible. The other two baseline alloys measured as expected.

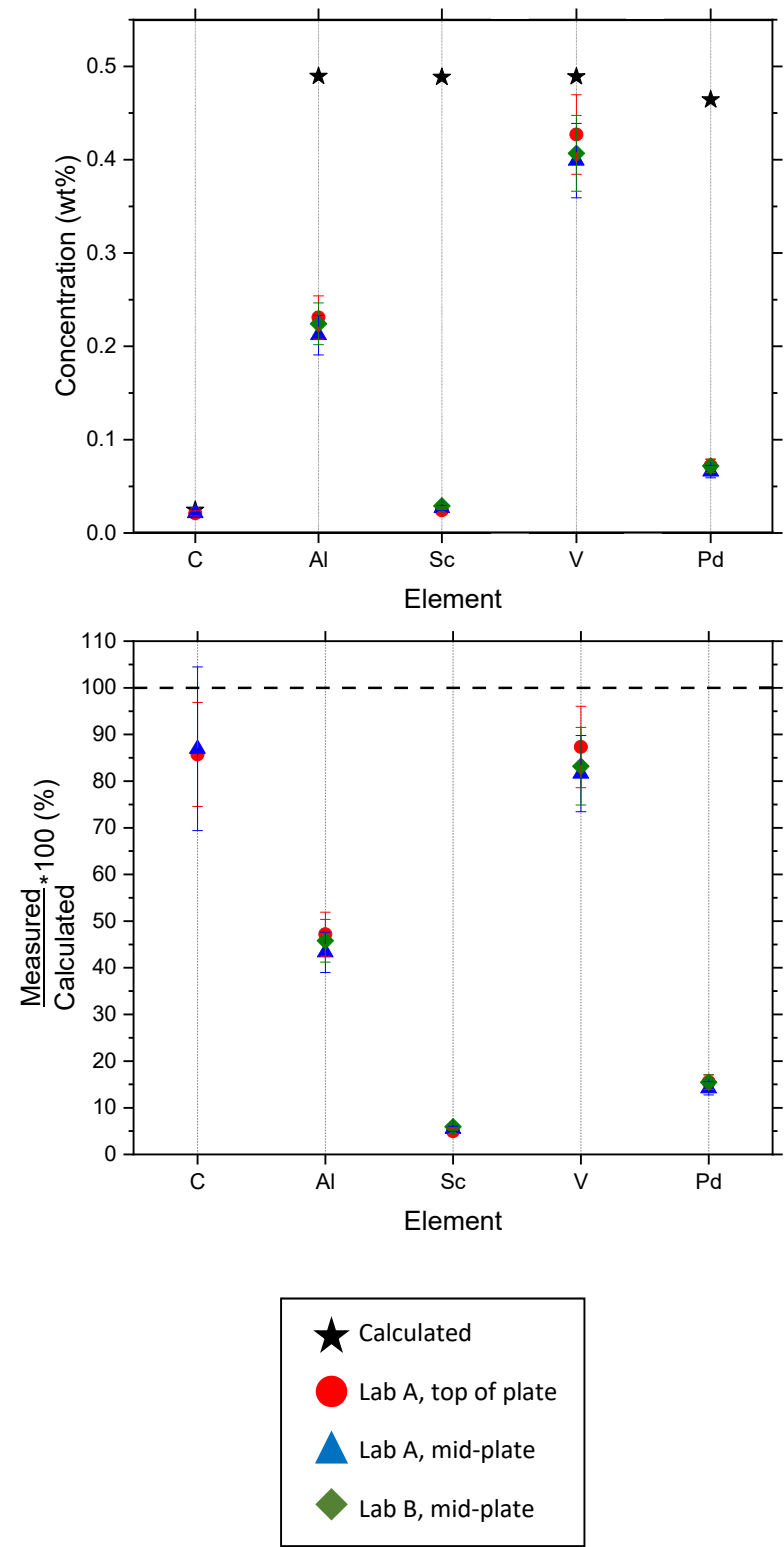
All the chemistry results from the four baseline alloys are plotted in **Figure 3.3**. The black stars represent the calculated values, the red circle are Lab A's measured values from the top of the plate, the blue triangle is Lab A's measured values from mid-plate, and the green diamond is Lab B's measurement from mid-plate. The top plot in each displays the calculated and measured concentration of each taggant element along with carbon in weight percent. The calculated values were based on the weights of the individual elements that were added to both the master alloy button and the VIM casting. Most of the taggant elements were added close to the proposed 0.5 wt% value except for Ir. Ir was only added to 0.36 wt% due to source material limitations. The bottom plot normalizes the measured values with the calculated values. In other words, the bottom plot shows what percentage of the taggant element made it into the casting. The symbols in the chemistry plots often fall on top of each other, so please refer to the appendix for the actual values.

To access detectability and manufacturability, chemistry results from the four baseline alloys can be analyzed together. Concerning detectability, measurements from the two laboratories should be compared, the blue triangle and the green diamond in **Figure 3.3**. There was no significant difference between measurements from the two laboratories within 10% uncertainty. For manufacturability, the conclusions remain the same as those described in the previous work Section 3.3. There was no significant difference between the middle and the top of the castings (red circles vs. blue triangles), but most of the taggant elements measured lower than their anticipated value. This does not rule out any of the elements as possible chemical taggants. However, Sc and Tb are questionable since less than 10% of these elements made in into the final product. Also, the investigation into the taggant elements in 19C1-016 (Ni, Ge, Ce, and Ta) will end here. Any results from this alloy are questionable due to the reaction in the crucible. Given more time, these elements should still be investigated as possible taggants starting with determining which element, or combination of elements, reacted in the crucible. So, twelve elements are still in consideration as chemical taggants with two of them being questionable.

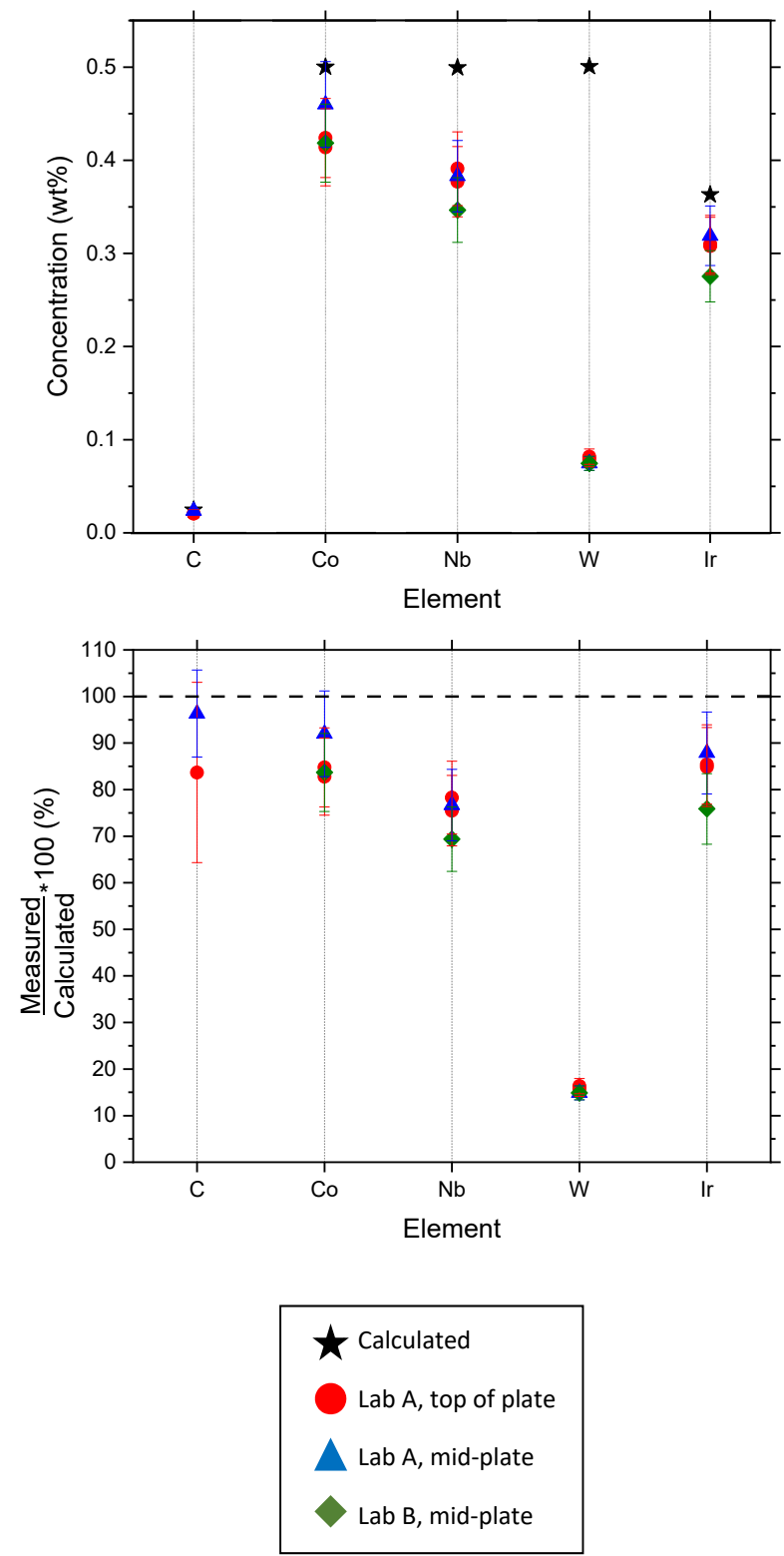
(a) 19C1-010 : baseline alloy



(b) 19C1-014 : baseline alloy



(c) 19C1-015 : baseline alloy



(d) 19C1-016 : baseline alloy

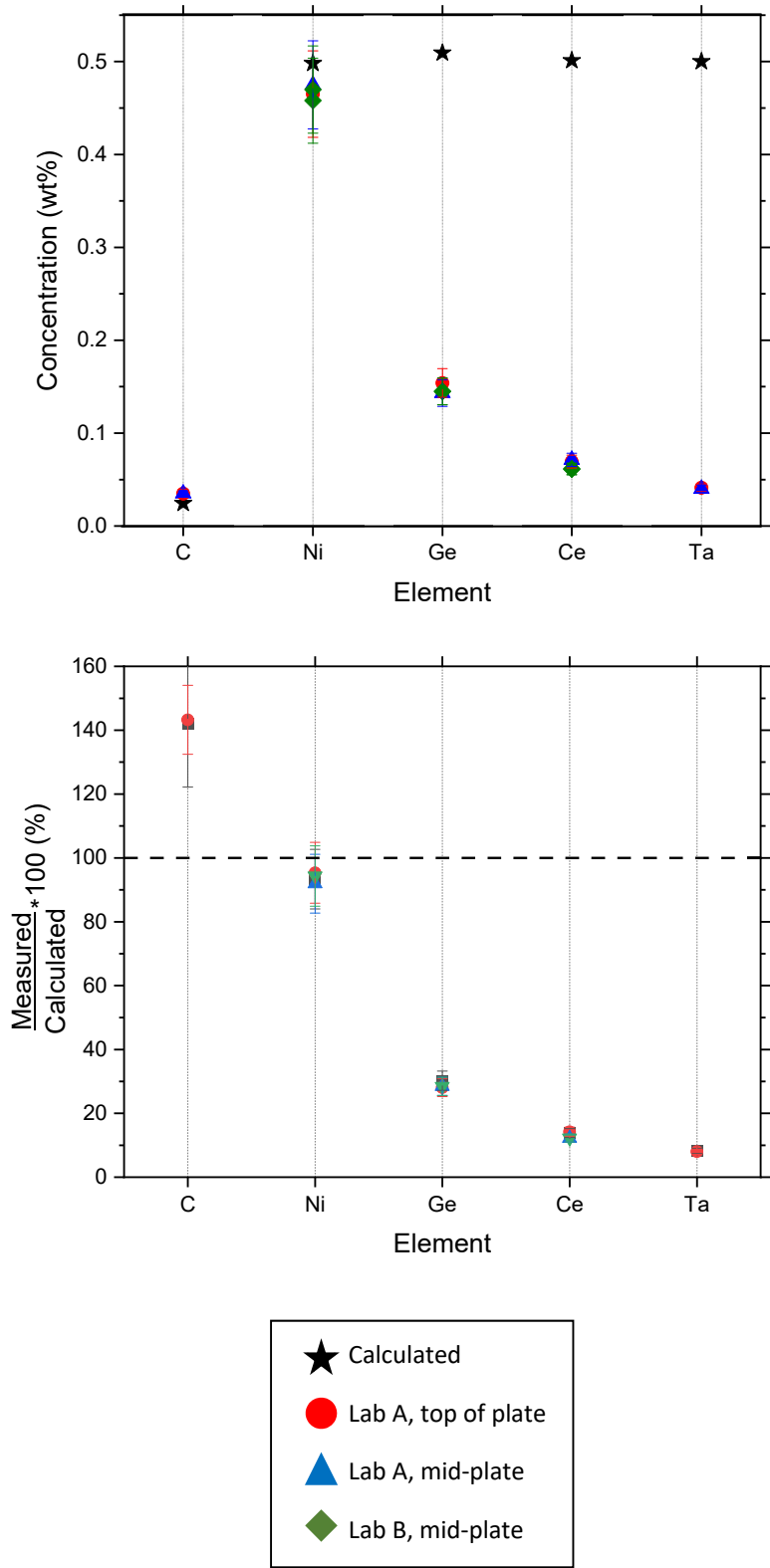


Figure 3.3 (images (a)-(d) on preceding pages). Chemistry analysis from baseline castings. The top plot presents the measured and calculated values of each element in weight percent. The second plot normalizes each measured value by the calculated value, so if an element measured at the same amount as was expected, it would lie at 100%. For each baseline alloy, no major chemical difference can be seen in casting location or in the different laboratory measurements. Most of the chosen taggant elements measured lower than their expected calculated value.

3.4.2. Secondary phase segregation – microscopy results

To continue investigation of second phase segregation as a viable tagging strategy, microstructural analysis was performed using LOM and SEM along with EDS for qualitative localized chemical analysis. The first baseline alloy, 19C1-010, is summarized in the prior work section 3.3.3. Similar to 19C1-010, nine samples were examined with LOM along the height of both 19C1-014 and 19C1-015. There was no significant difference in the microstructure along the height of each plate, so three samples per plate were down selected for further characterization via SEM and EDS. Since 19C1-016 reacted with the crucible during casting, this alloy was not characterized further.

Al, Sc, V, and Pd were the taggants purposely added in baseline alloy 19C1-014. Al and Pd were expected to form intermetallics. V was anticipated to incorporate into uranium carbides while Sc was expected to be found in oxide form. Representative back-scatter electron (BSE) images from the (a) hot top, (b), mid-plate, and (c) bottom of the plate are shown in **Figure 3.4**. The various phases are labeled with their elemental makeup that was determined via EDS. Three different second phases were commonly found in 19C1-014. A scandium oxide phase was found, as expected. Sc was also found in a globular-shaped intermetallic phase along with Al and Pd. Another intermetallic phase containing Al, V, and small amounts of Pd formed elongated particles throughout the plate. While it was anticipated that Al and Pd would form intermetallics, V was expected to incorporate into uranium carbides, which was not observed. This was likely due to higher-order interactions on the phase diagram and/or non-equilibrium solidification structures.

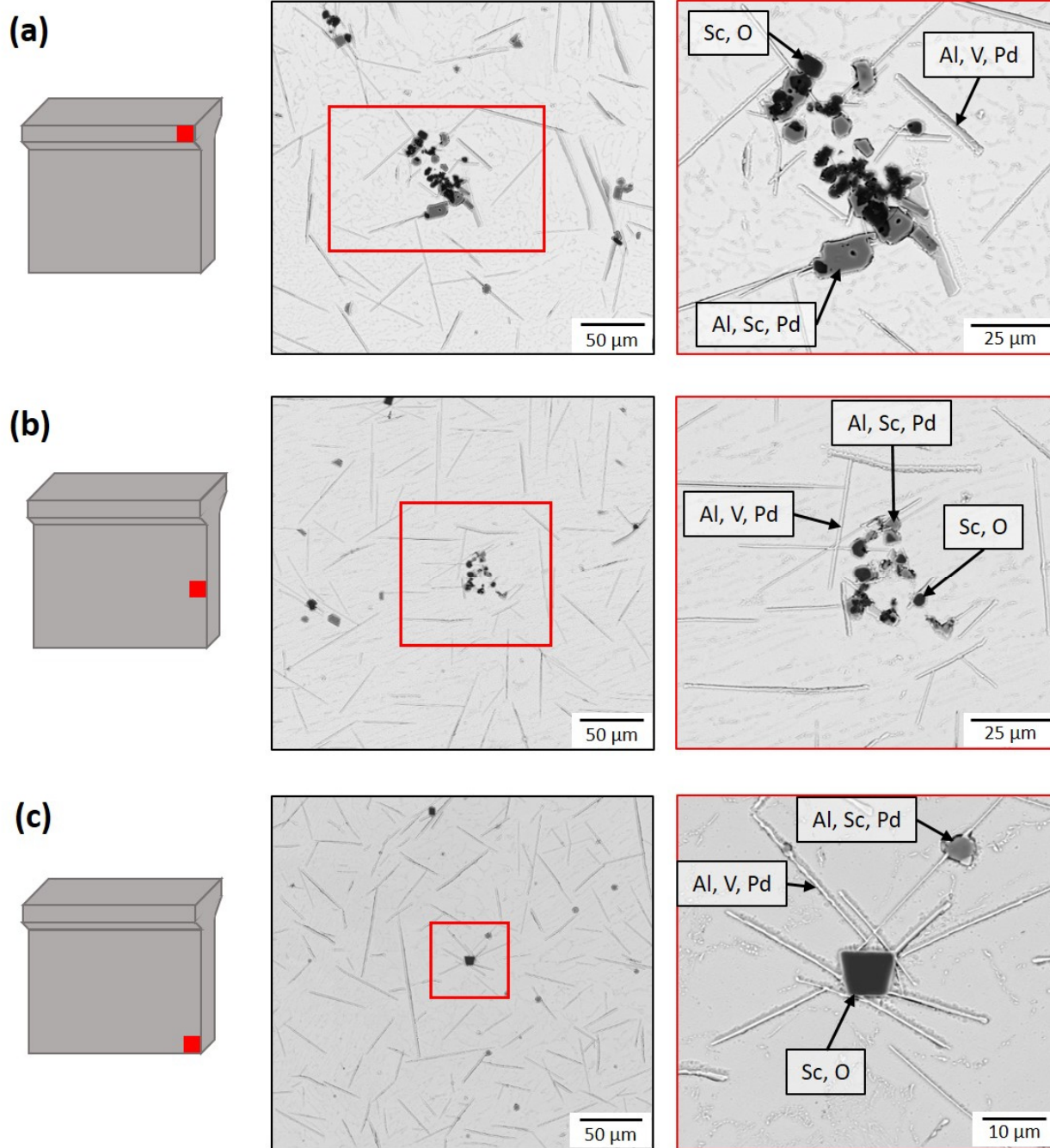


Figure 3.4. Representative BSE-SEM images taken from the (a) hot top, (b) middle, and (c) bottom of 19C1-014. Three different second phases can be seen along the length of the plate including a Sc oxide phase, and two different intermetallic phases forming elongated and globular particles.

Co, Nb, W, and Ir were the taggants present in 19C1-015. Co and Ir were expected to form intermetallic phases while W and Nb were anticipated to form carbides, nitrides, and/or oxides. BES-SEM images from the (a) hot top, (b) middle, and (c) bottom of the plate are shown in **Figure 3.5** with the elements in the phases labeled. Note that images (a) and (b) were taken at a different contrast level than (c), which is why the same phases appear much darker in (c) than in the other two images. Similar phases were found in each location that was analyzed. Co was found in a phase, likely U_6Co , which appeared along grain boundaries. This phase was outlined with uranium carbide, which is visible in both (a) and (c). At times, an oxide layer appeared between the U_6Co and carbide. Nb was also found, as expected, in faceted carbide particles throughout the casting. It was also incorporated in some uranium carbide particles as well. In the three samples there were analyzed in the SEM, Ir and W were not found in any second phase particles. Based on this result, these two elements would no longer be considered suitable taggants in regards to second phase segregation unless further investigation is done to determine where the two elements are located. It should also be noted that some oxide particles containing Tb and Sc were found in this alloy. They were not purposefully added in this casting. This is evidence of cross-contamination that likely occurred during the processing of the master button alloys. All of the buttons were made in the same hearth, so cross contamination could occur.

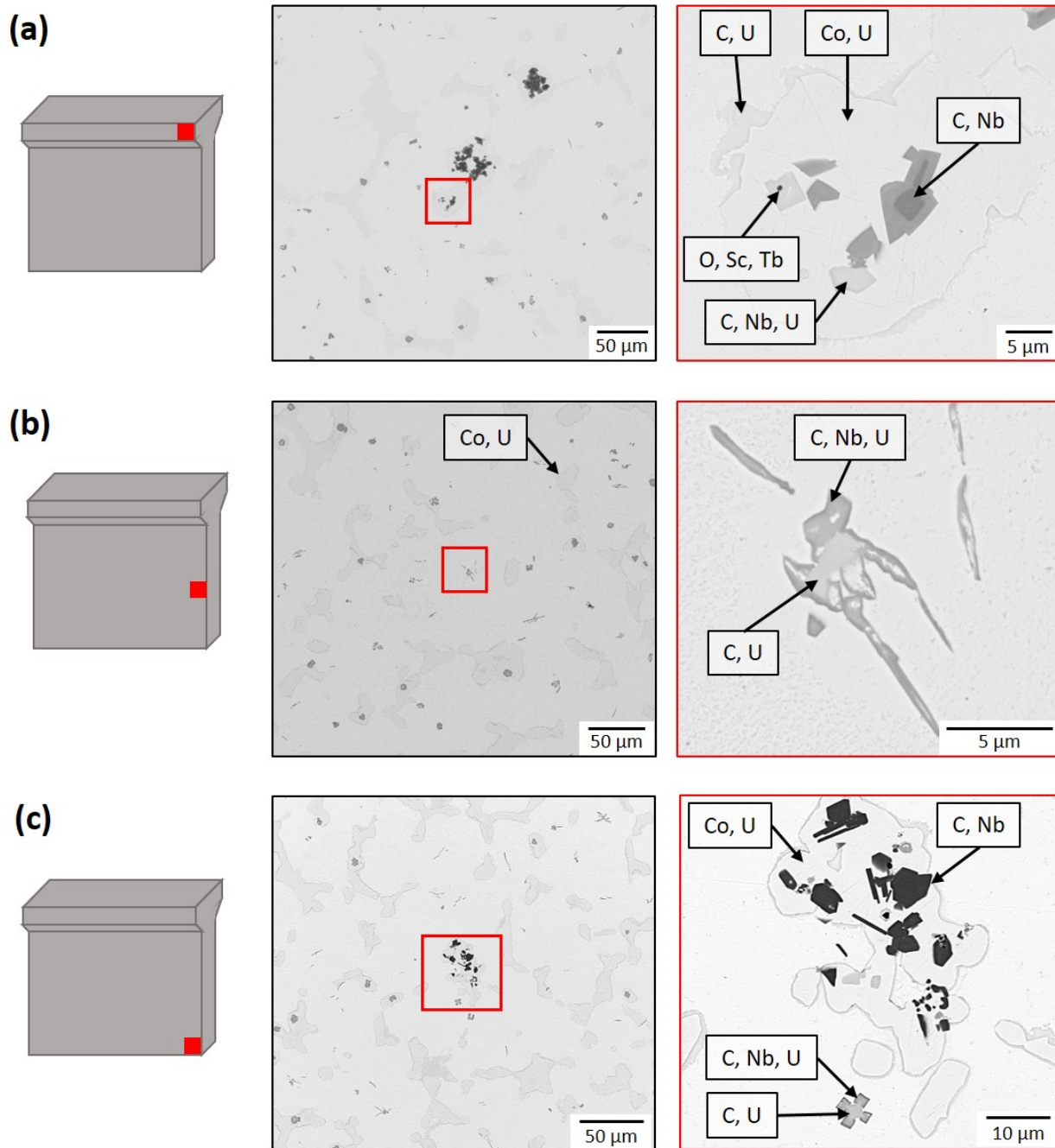


Figure 3.5. Representative BSE-SEM images taken from the (a) hot top, (b) middle, and (c) bottom of 19C1-015. Nb carbides and Co intermetallics are easily located throughout the plate. Sc and Tb oxide particles provide evidence of cross contamination that likely occurred during the processing of the master alloy buttons. W and Ir were unable to be found in any second phase particles via SEM.

3.4.3. Conclusions – baseline alloys

Based on the chemistry and microstructure analysis from the baseline alloys, both bulk metal tagging strategies are still viable options for a majority of the taggant elements. Ni, Ge, Ce, and Ta will need to be set aside for the time being. Further investigation is needed to determine what caused the processing issue.

The remaining 12 elements are still viable options to be added as taggants to bulk uranium in specific ratios. No significant difference in measurements between the two laboratories, so it appears as though all of the elements are detectable. There was also no significant macrosegregation in the castings. However, none of the elements achieved the calculated 1:1:1:1 ratio. This was likely due to poor mixing during processing, but most of the elements made it into the final alloy in some capacity. Sc and Tb were measured at less than 10% of their expected value, so these two are questionable as chemical taggants, but not yet completely ruled out.

A majority of the elements are still options for second phase taggant as well. Ten of the twelve elements were easily located in various second phases using SEM and EDS. V and Sc were found in unexpected second phases, but that is not a showstopper. W and Ir were not located with the microscopy tools used in this study making them questionable candidates for second phase taggants.

In summary, Sc and Tb are questionable candidates for chemical taggants while W and Ir are questionable for second phase taggants. The other elements, including Al, Ti, V, Mn, Co, Nb, Pd, and Au, are still in good standing for both taggant options.

3.5. FY21 activity – mixed/dilution alloys

3.5.1. Design and procedure

The next step in the bulk tagging investigation was to mix and dilute the baseline alloys with the goal of retaining the taggant ratio through another round of processing. Among a possible ten dilution and mixture combinations of the baseline alloys, four were chosen to move forward. Those combinations are shown in **Figure 3.6**. This resulted in three mixtures from the three successful baseline alloys in approximately a 1:1 ratio and one dilution alloy, a baseline alloy mixed with unalloyed DU in approximately a 1:1 ratio. The alloying elements are expected to become half of their initial values. So, if starting from a nominal 0.5 wt% in the baseline alloy, they will end up at 0.25 wt% in the mixed/dilution alloy.

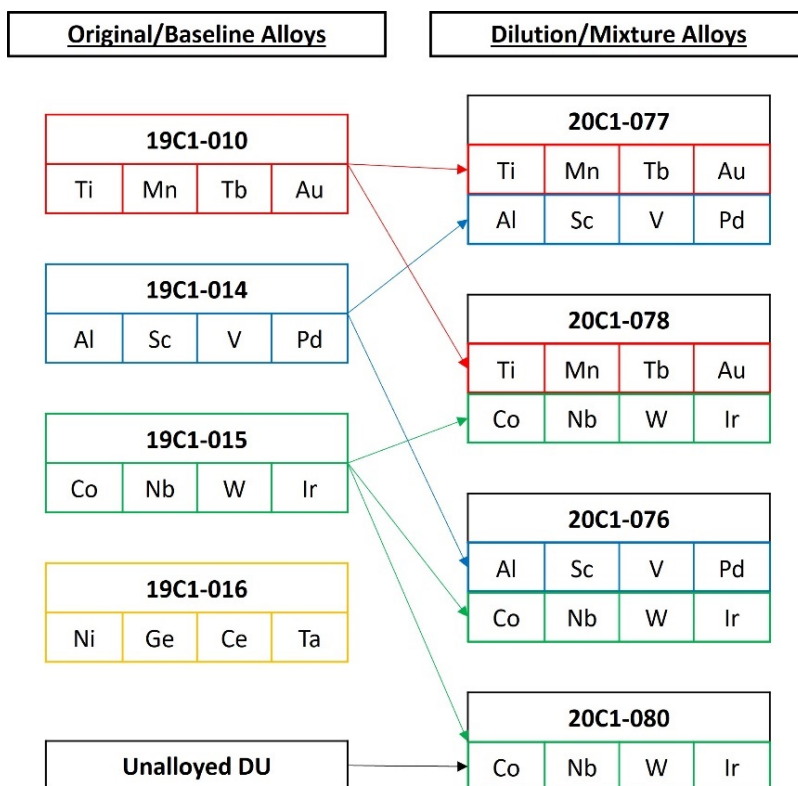


Figure 3.6. Schematic detailing the chosen dilution and mixtures of the original baseline alloys.

Figure 3.7 shows the workflow for this part of the study. The baseline alloys were split and set aside for casting. The mixed/dilution alloys were cast in a VIM furnace resulting in four plates, similar to the baseline alloys. The plates were then sectioned for metallography, and machine turnings were taken for chemical analysis. Chemical samples were taken from two locations per casting, the middle and the top of the plate. The samples were also analyzed at two different LANL laboratories, same as the baseline alloys. Details of these steps follow.

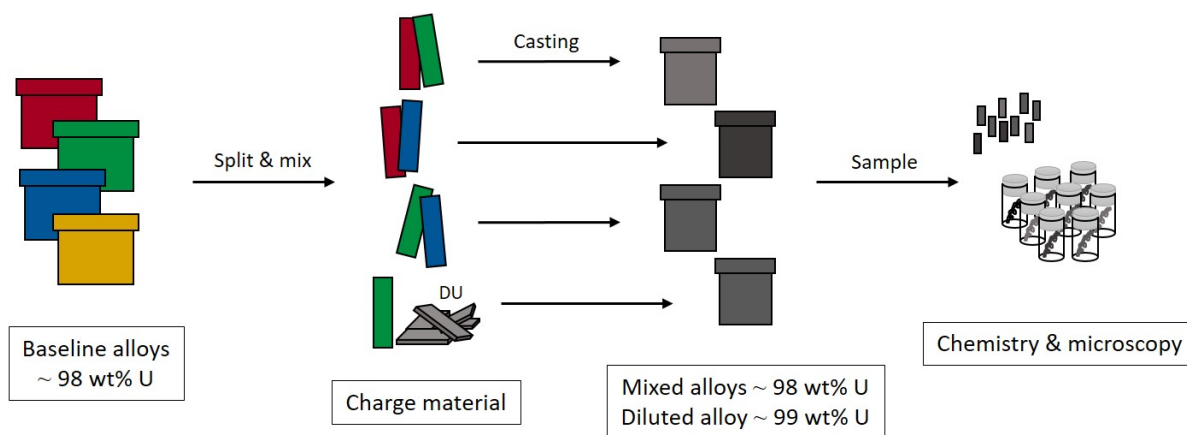


Figure 3.7. Schematic showing the processing of the mixed/diluted alloys.

3.5.2. Casting outcomes

The four mixed/dilution alloys were cast in 6" tall, 6" long, and 0.35" thick plate molds in a VIM furnace. The furnace setup used for these castings is shown in **Figure 3.8**. The charge makeup for each casting is shown in **Table 3.3** along with basic casting information. Images of all the as-cast plates are shown in **Figure 3.9**. Since the goal was to combine the two baseline materials evenly, the total charge mass for some of the castings was less than what the mold was designed for, resulting in a variety of hot top sizes across the four castings. However, each casting appeared visually sound.



Figure 3.8. The furnace setup that was used for the mixed/dilution alloys.

Table 3.3. Casting ID, charge makeup, and other casting details for the four mixed/dilution uranium alloys.

Casting ID	Charge		Casting date	Charge mass (g)	Casting mass (g)	Casting yield (%)
	Material	Mass (g)				
20C1-076	19C1-014	2883	11/05/2020	5723	5410	94.53
	19C1-015	2840				
20C1-077	19C1-010	2239	11/09/2020	4458	4254	95.42
	19C1-014	2219				
20C1-078	19C1-010	2015	11/10/2020	4043	3874	95.82
	19C1-015	2028				
20C1-080	19C1-015	2483	11/17/2020	4970	4639	93.34
	DU	2487				

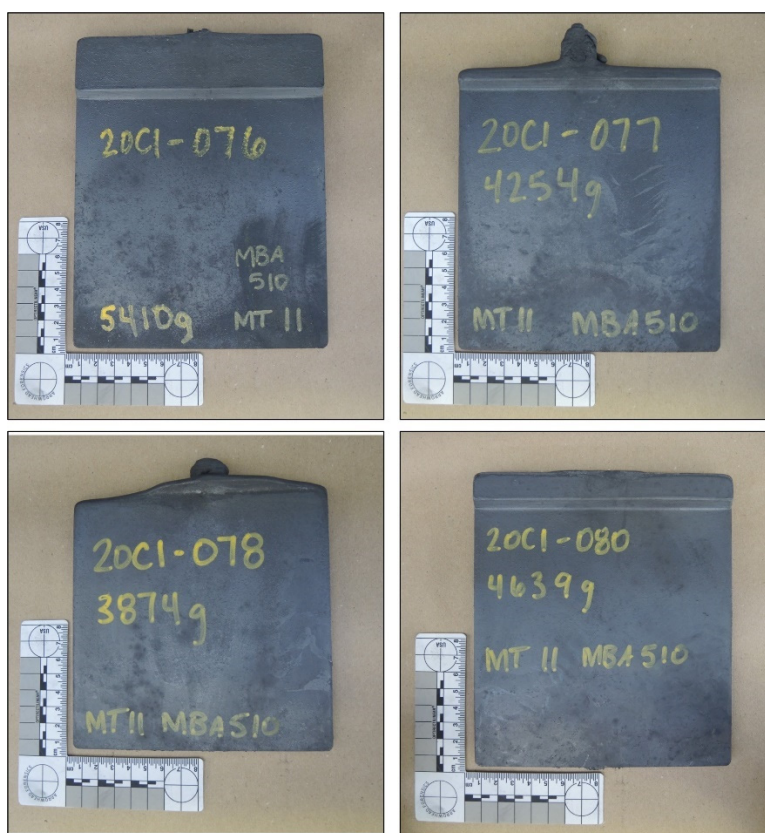


Figure 3.9. Photos of the as-cast mixed/dilution alloys. Each casting visually appeared sound. The goal of combining two of the baseline alloys evenly resulted in a variety of charge masses which is apparent in the variety of hot top heights.

A slice was taken from the edge of each of the four mixed/dilution alloys and subsequently cut up for microstructure analysis. Of the five total samples cut from each plate, three were fully characterized: the samples labeled a, c, and e in **Figure 3.10**. The characterized samples were taken an inch from the bottom, an inch around the center of the plate, and an inch from the top of the plate. With the inconsistent hot top heights, the top sample could have been all hot top, such as 20C1-076, or the top of the plate, such as 20C1-078. This is shown in **Figure 3.10**. Also, two locations per plate were sampled for chemical analysis: the middle of the plate and the middle of the top of the plate.

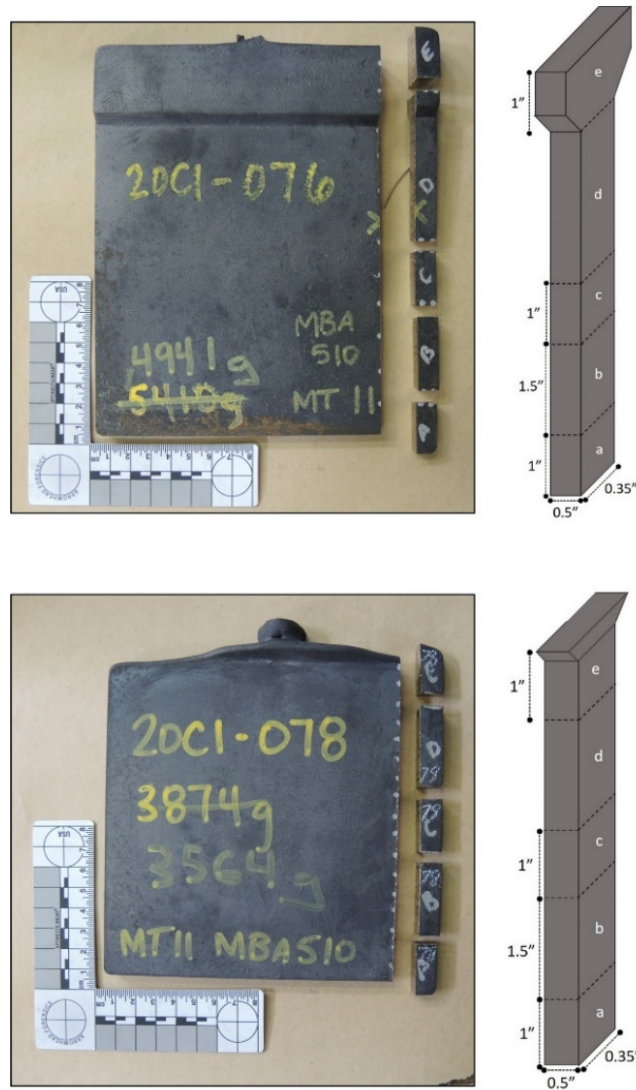


Figure 3.10. Two plates showing the cut-up plans for the mixed/dilution alloys. Samples labeled a, c, and e were fully characterized with LOM, SEM, and EDS. With the various hot top heights, sample e taken from the top of the plate could have been all hot top, such as 20C1-076, or just the top of the plate, such as 20C1-078.

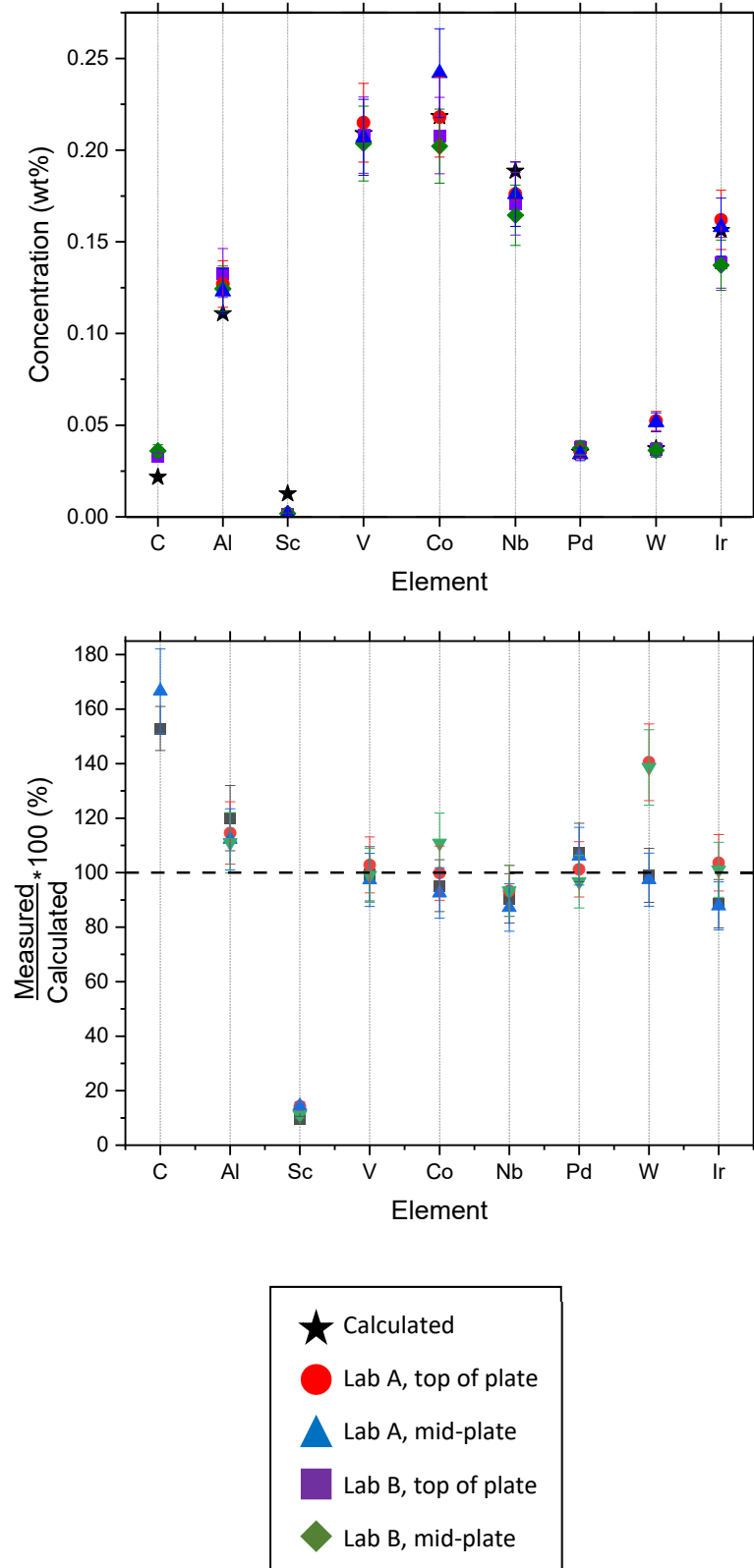
3.5.3. Addition of elements in specific ratios – chemistry results

As was stated earlier, when it comes to the addition of elements in specific ratios, two things are important: manufacturability and detectability. Similar to the baseline alloys, bulk chemical analysis via ICP-MS was performed at two different laboratories at LANL, and each alloy was sampled from two different locations, the top of the plate and mid-plate. Chemistry results from the four mixed/dilution alloys are plotted in **Figure 3.11**. The top plot on each figure displays the calculated and measured concentration of each taggant element along with carbon in weight percent. Measured concentration values from the baseline alloys along with charge weight was used to calculate the expected chemistries for the four mixed/dilution alloys. The bottom plots in **Figure 3.11** normalizes the measured values with the calculated values. In other words, the bottom plot shows what percentage of the taggant element made it into the casting. In each plot, the black stars represent the calculated values, the red circles are Lab A's measured values from the top of the plate, the purple squares are Lab B's measurement from the top of the plate, the blue triangle is Lab A's measured values from mid-plate, and the green diamond is Lab B's measurement from mid-plate. All the values are reported in the appendix.

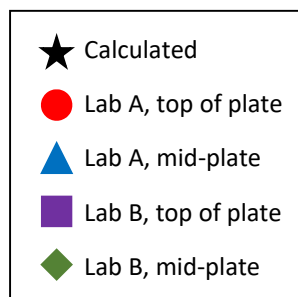
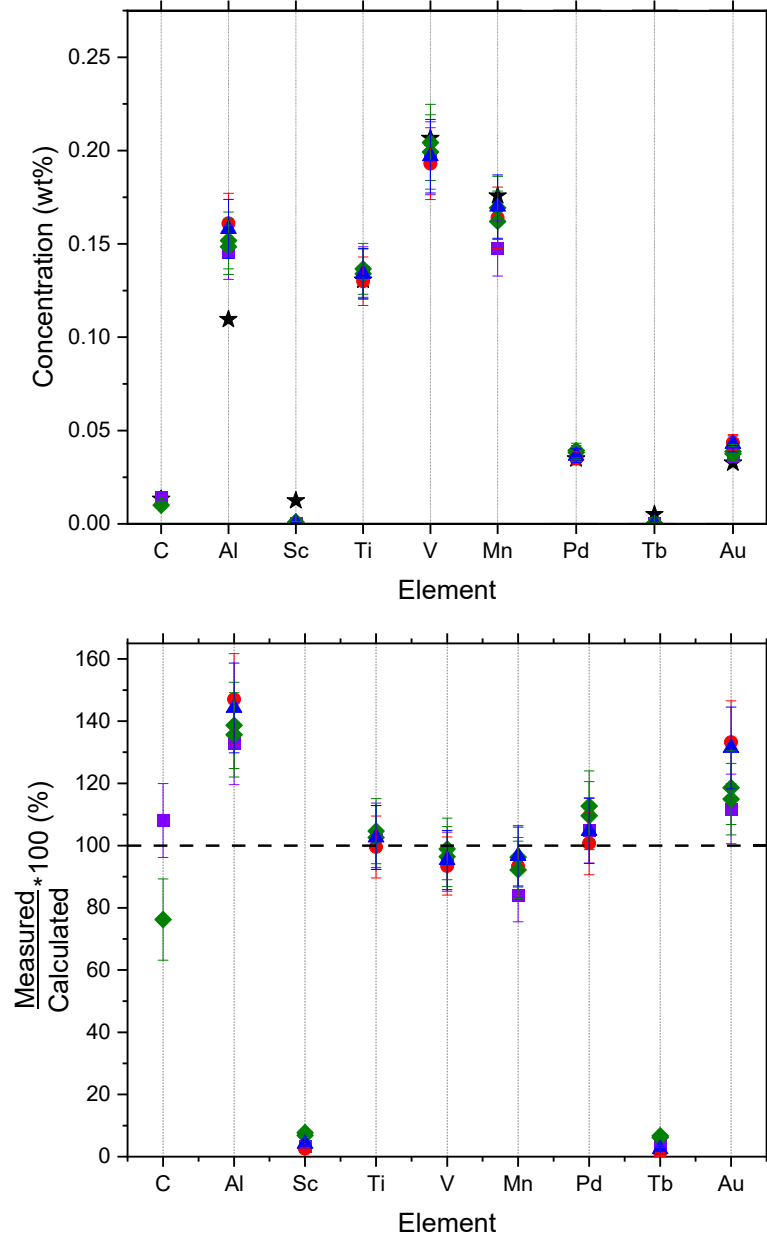
Comparing results from the two labs for detectability, W and Ir had noticeable differences in each of the three alloys they were present in **Figure 3.11 (a, c, d)**. This raises concerns for these two elements as chemical taggants. If the measurements are not repeatable across laboratories, the elements are not suitable as chemical taggants. For manufacturability, there was no significant difference in measurements from the different locations in each alloy, so it seems as though segregation in the final product is not a concern with the elements investigated here. Since each of the taggant elements were already well mixed in the charge material, the mixed/dilution alloy results should give a better indication as to whether or not an element will make it through processing and into the final part.

In the baseline alloys, Sc and Tb were of concern, and they presented an issue in the mixed alloys as well. Less than 15% of the anticipated amount was measured in all the alloys containing Sc and/or Tb, shown in **Figure 3.11 (a-c)**. This rules them out as possible chemical taggants unless more work is done. Ti measured slightly lower than anticipated in 20C1-078, **Figure 3.11 (c)**. Al and Au measured slightly higher than expected, **Figure 3.11 (a-c)**. Since it is unlikely that Au was added (e.g., as a cross-contaminant) in during the mixed alloy processing, this difference could be attributed to possible issues with detection. As for the Al, its high, unintended level of ~800 wppm in one of the parent materials, 19C1-010, can explain most of the higher-than calculated value in 20C1-077, **Figure 3.11 (b)** (recall the calculation did not take into account the chemical analysis results from Lab B; see appendix). The issues with Sc, Tb, and Au should be investigated further before drawing any conclusions. The other tagging elements looked normal: Ti, V, Mn, and Pd.

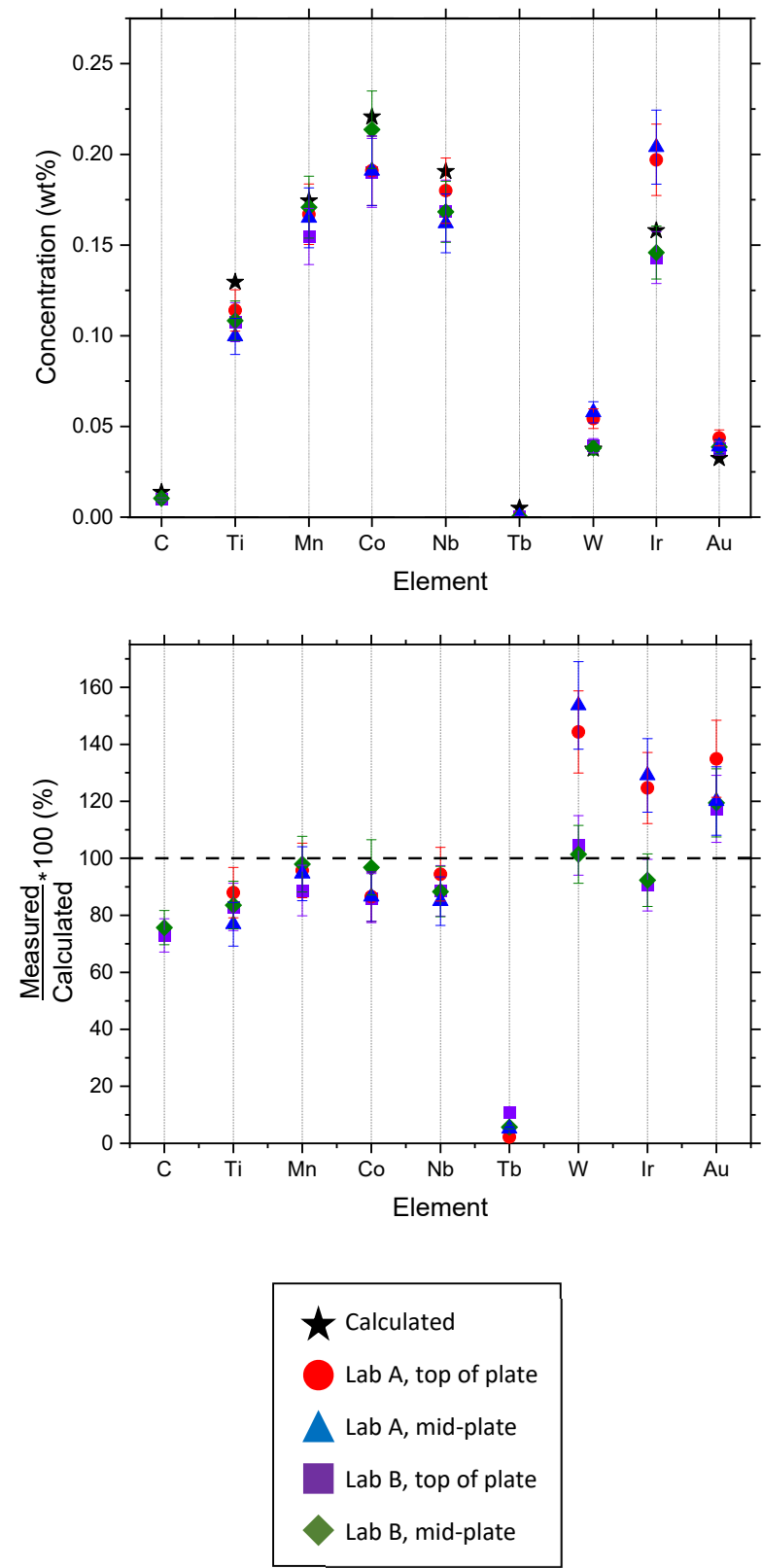
(a) 20C1-076 : mixed alloy



(b) 20C1-077 : mixed alloy



(c) 20C1-078 : mixed alloy



(d) 20C1-080 : dilution alloy

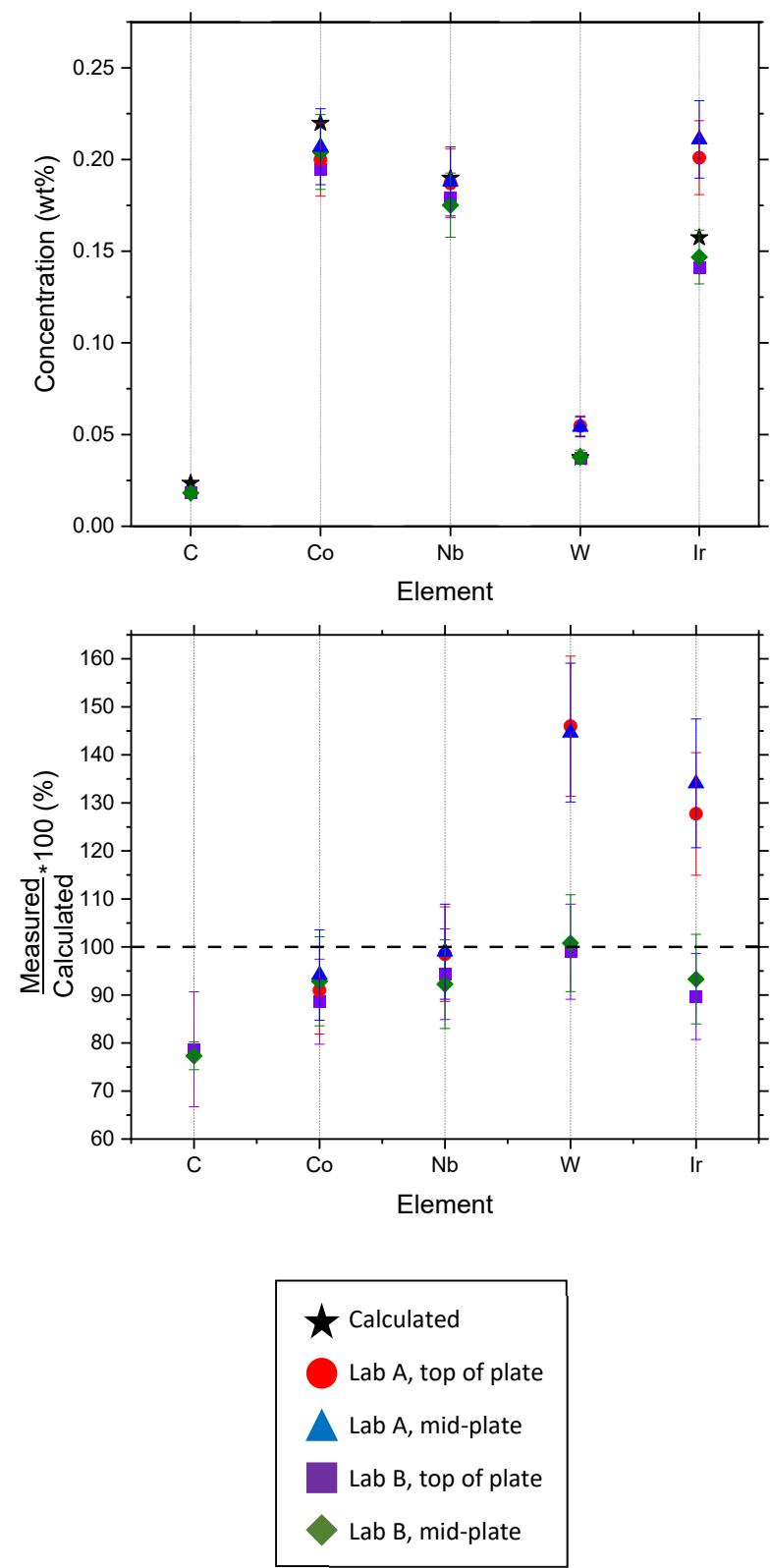


Figure 3.11 (images (a)-(d) on preceding pages). Chemistry analysis from the mixed castings and the dilution casting. The top plot presents the measured and calculated values of each element in weight percent. The second plot normalizes each measured value by the calculated value, so if an element measured at the same amount as was expected, it would lie at 100%. No major chemical difference can be seen between casting location. There is a difference in the measured values of W and Ir between the two different laboratories. Except for Tb and Sc, the measured values of the elements do not differ nearly as much from their calculated values as was seen in the baseline alloys.

To determine if any elemental taggant ratios survived further material processing, chemical results from the baseline alloys can be combined with the measurements from the mixed/dilution alloys. With Sc, Tb, W, and Ir removed for reasons described earlier, seven binary elemental ratios are left to assess, and they are plotted in **Figure 3.12** and listed in Table 3.4. The ratio from the baseline alloys are represented with black squares, the red circles are ratios from the mixed alloys while the blue triangle is the ratio calculated from the dilution alloy. See the calculated numbers in the appendix for a closer look. The ratios of the seven binary combinations are reasonably stable, but these numbers provide nothing conclusive. The error used here is approximately 14% of the calculated ratio based on uncertainty propagation. This needs to be better defined in order to draw any strong conclusions from the elemental tagging ratios. With the work presented here, the measurements of the individual elements are a better way to access how applicable they are for use as a taggant.

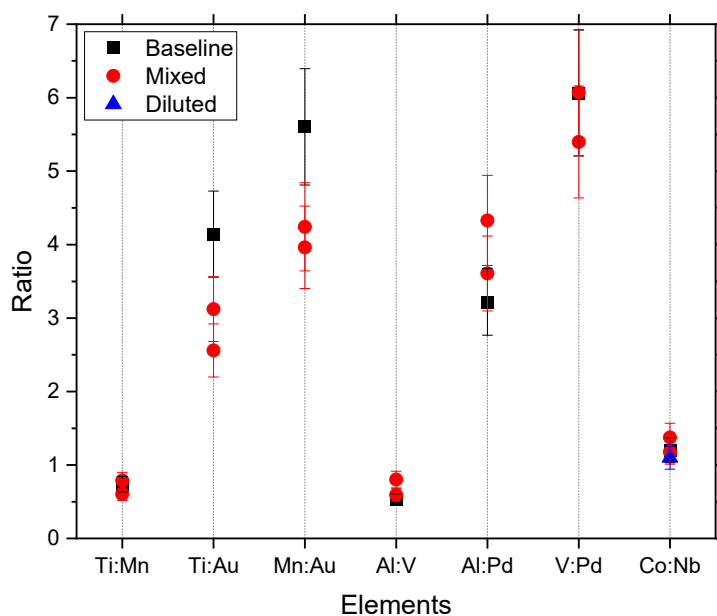


Figure 3.12. The elemental tagging ratios calculated for seven binary combinations. While the ratios appear reasonably stable, nothing conclusive can be said until more effort has been spent on error analysis.

Table 3.4. The elemental tagging ratios calculated for seven binary combinations, as displayed in Figure 3.12.

Elemental Ratios (based on weight assays)								
	Baseline alloys		Mixed alloys		Mixed alloys		Dilution alloy	
Elements	Ratio	Error	Ratio	Error	Ratio	Error	Ratio	Error
Ti : Mn	0.739	0.105	0.788	0.111	0.604	0.0854		
Ti : Au	4.14	0.586	3.12	0.442	2.56	0.362		
Mn : Au	5.60	0.792	3.96	0.560	4.24	0.600		
Al : V	0.531	0.0751	0.594	0.0840	0.802	0.113		
Al : Pd	3.22	0.456	3.61	0.510	4.33	0.612		
V : Pd	6.06	0.858	6.07	0.858	5.40	0.763		
Co : Nb	1.20	0.170	1.38	0.194	1.18	0.167	1.10	0.156

3.5.4. Secondary phase segregation – microscopy results

As described above, when adding alloying elements to metal, second phase particles will form resulting in a secondary tagging strategy. Three samples taken from the top, middle, and bottom of each of the mixed/dilution alloys were examined via LOM and SEM/EDS. There was no significant difference between the locations in each plate in either microstructure or qualitative chemistry of the phases.

Mixed alloy 20C1-076 is a combination of the two baseline alloys 19C1-014 (Al, Sc, V, Pd) and 19C1-015 (Co, Nb, W, Ir). **Figure 3.13** shows representative BSE-SEM images from the (a) top, (b) middle, and (c) bottom of the plate. As expected, various intermetallic phases were found. One phase throughout the plate contained Al, Co, and Ir. Recall, Ir could not be located in the baseline alloy. Another intermetallic phase present were in elongated particles that contained Nb, Al, and V. V was expected to incorporate into uranium carbides while Nb was expected to form its own carbide, as it did in the baseline alloy. Some of these elongated particles did contain Pd as well. One other intermetallic was the Co-containing phase, likely U_6Co , which was seen in the baseline alloy. It was outlined with uranium carbide along with an oxide in some locations. Sc formed an oxide phase as anticipated. W, however, was not found.

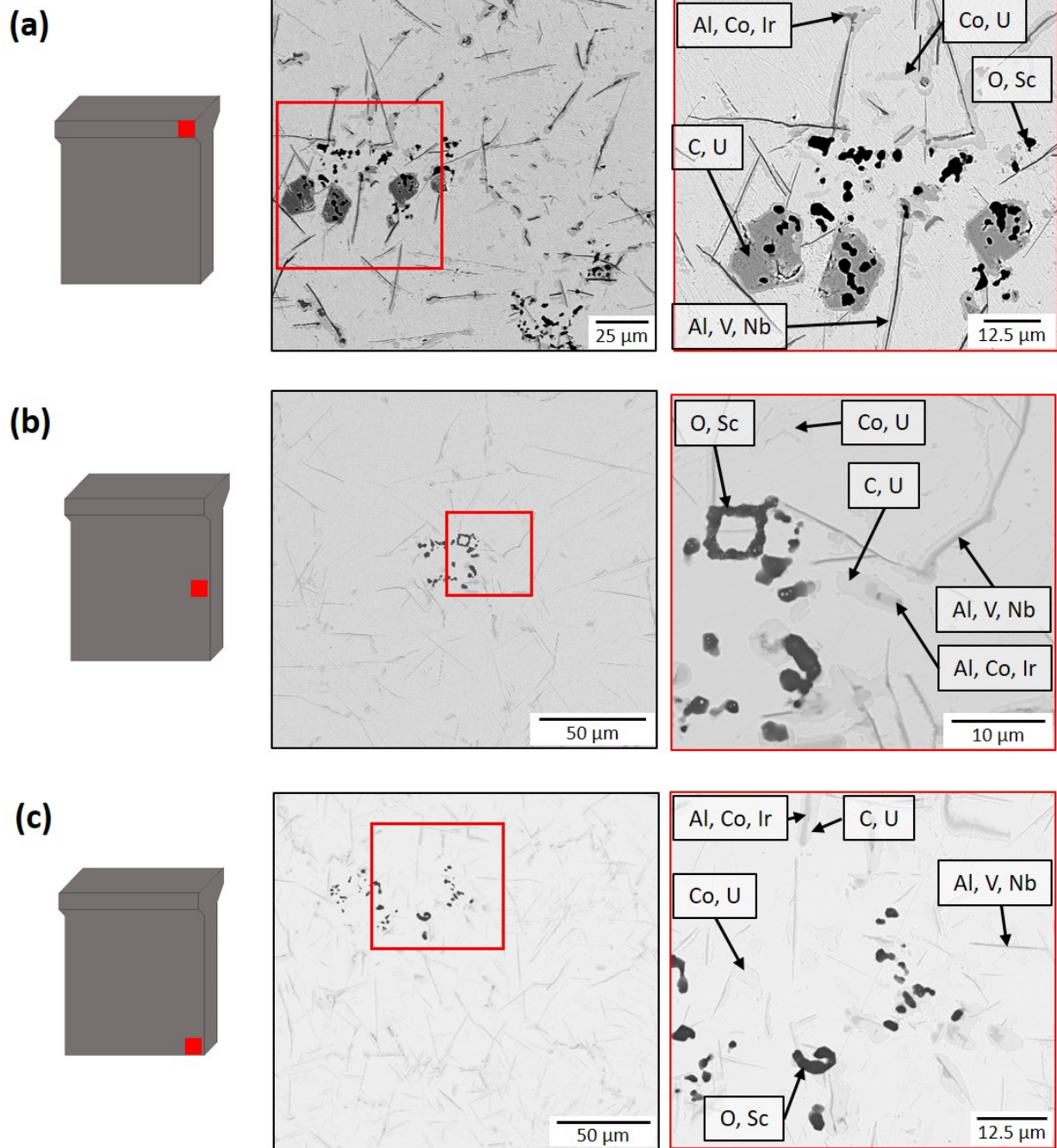


Figure 3.13. Representative BSE-SEM images taken from the (a) hot top, (b) middle, and (c) bottom of 20C1-076. Inset in low magnification images on left are shown in the higher magnification images on the right. Intermetallic phases of various chemistries and Sc-containing oxides are found throughout the plate. W was unable to be located in any of the second phases via SEM.

Mixed alloy 20C1-077 is a combination of 19C1-010 and 19C1-014. **Figure 3.14** shows representative BSE images from the (a) top, (b) middle, and (c) bottom of the casting. Carbides

containing Ti and V were ubiquitous throughout all three locations. It was anticipated that V would incorporate into uranium carbides, but it incorporated into the titanium carbides instead. As expected, Sc and Tb were found in an oxide phase throughout the plate. The remaining taggant elements, Al, Mn, Pd, and Au, formed an intermetallic phase that was found throughout the plate.

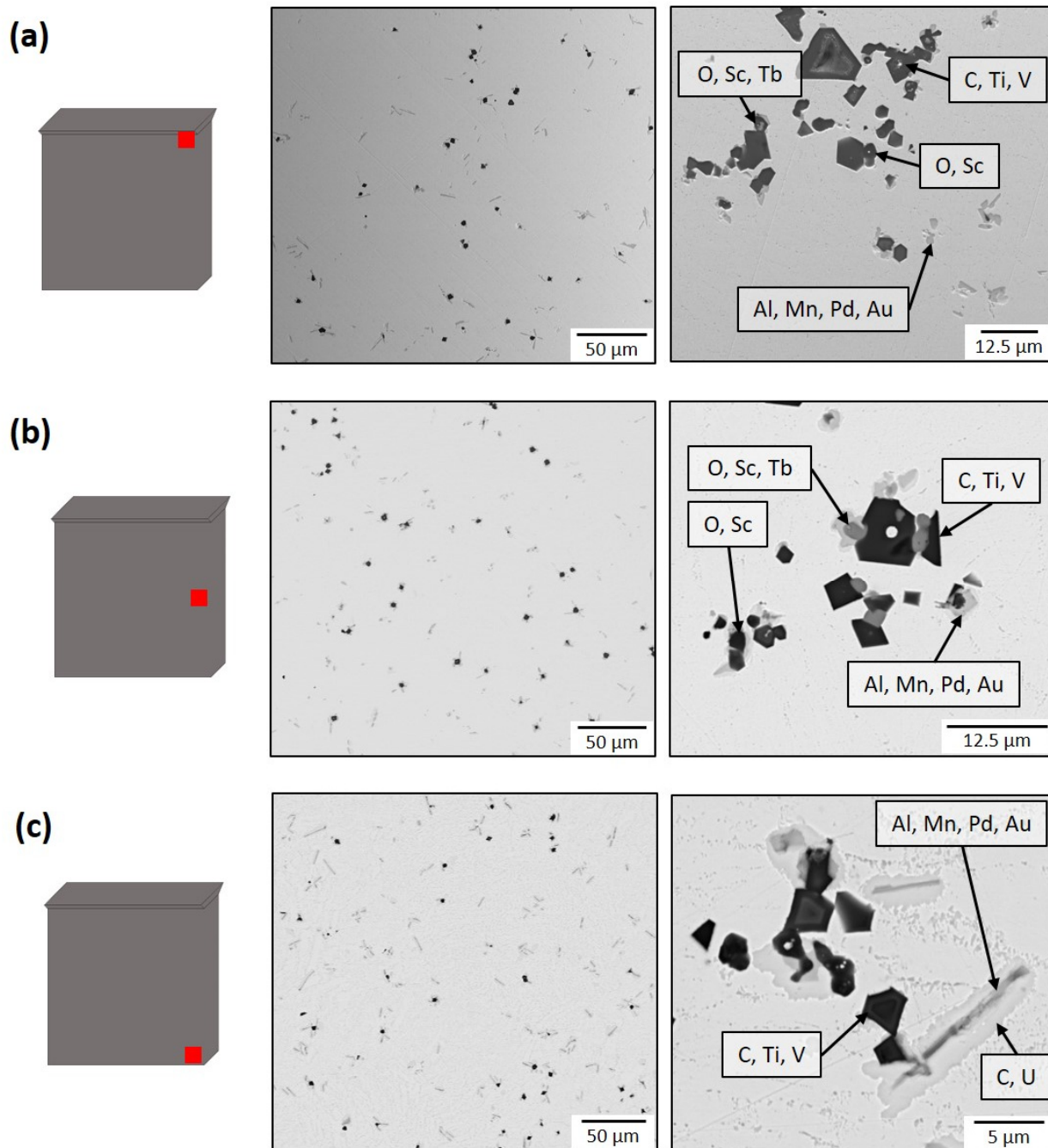


Figure 3.14. Representative BSE-SEM images taken from the (a) top, (b) middle, and (c) bottom of 20C1-077. Ti and V containing carbides, Tb and Sc oxides, and an intermetallic phase containing Al, Mn, Pd, and Au could be easily located throughout the plate.

20C1-078 is the mixed alloy formed from 19C1-010 and 19C1-015. **Figure 3.15** shows representative BSE images from the (a) top, (b) middle, and (c) bottom of the mixed alloy plate. Carbides containing Ti and Nb along with Tb and Sc oxides can be found throughout the casting, as expected. The Co-rich intermetallic phase is present, similar to the baseline alloy, but it now also contains Mn. This phase is still outlined in uranium carbide along with locations of oxide. Au and Ir form small intermetallic particles that can be found throughout the plate. The final two taggant elements, Au and W, were not located. In EDS, the peaks to identify Nb and Au overlap, causing detection issues, so this is likely the reason why Au was not properly identified.

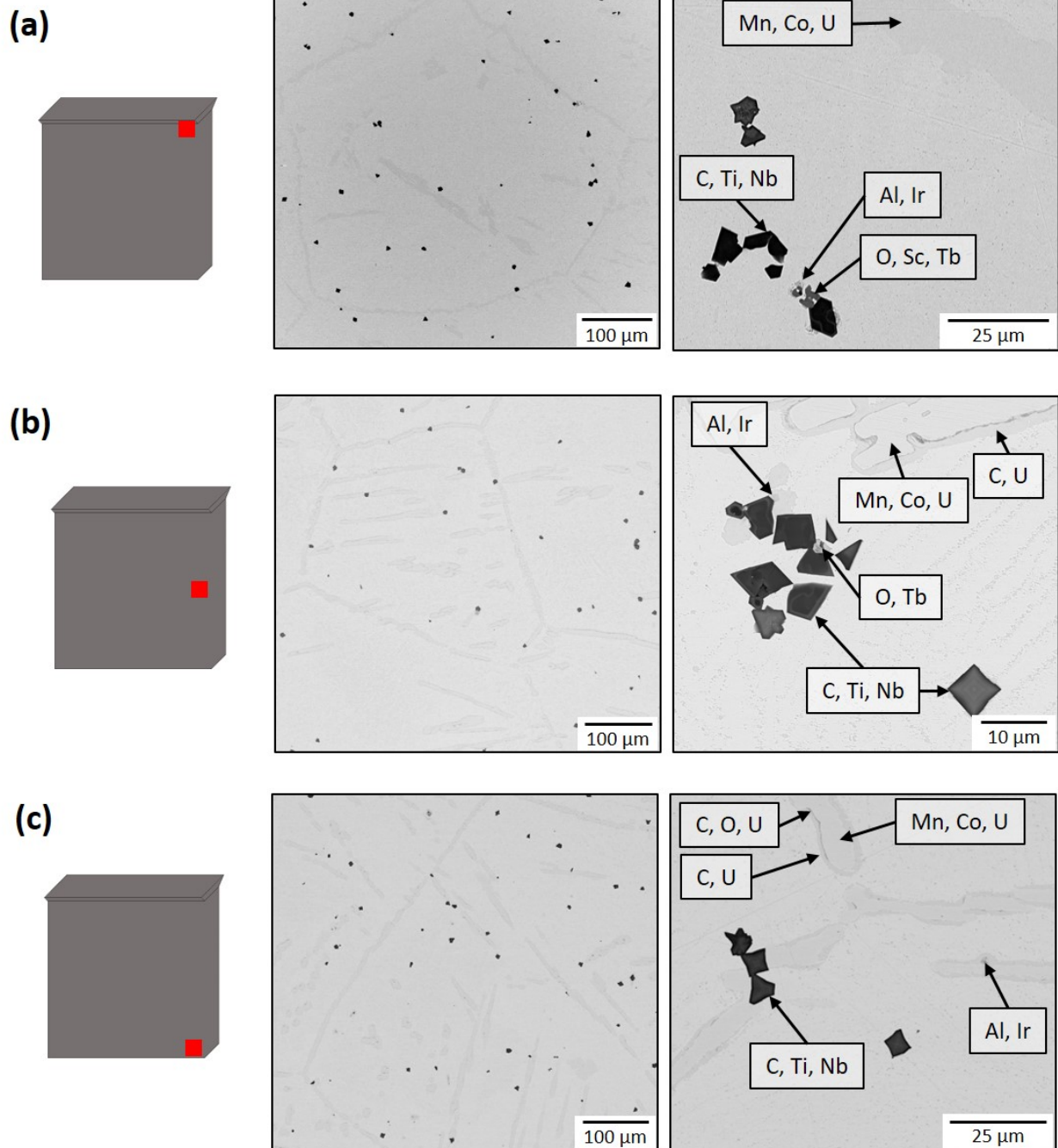


Figure 3.15. Representative BSE-SEM images taken from the (a) top, (b) middle, and (c) bottom of 20C1-078. Ti and Nb containing carbides, Tb and Sc oxides, and various intermetallic phases were found throughout the casting.

20C1-080 was the one dilution alloy produced at a 1:1 ratio of 19C1-015 and unalloyed DU.

Figure 3.16 shows representative BSE images from the (a) top, (b) middle, and (c) bottom of the casting. Nb carbides and a Co-rich intermetallic phase were found throughout the three samples analyzed. The Co intermetallic was outlined in uranium carbide and partially outline in

oxide. This structure was easiest to see with the surface finish of (c) the bottom sample. As with the baseline alloy, Ir and W could not be detected with SEM/EDS.

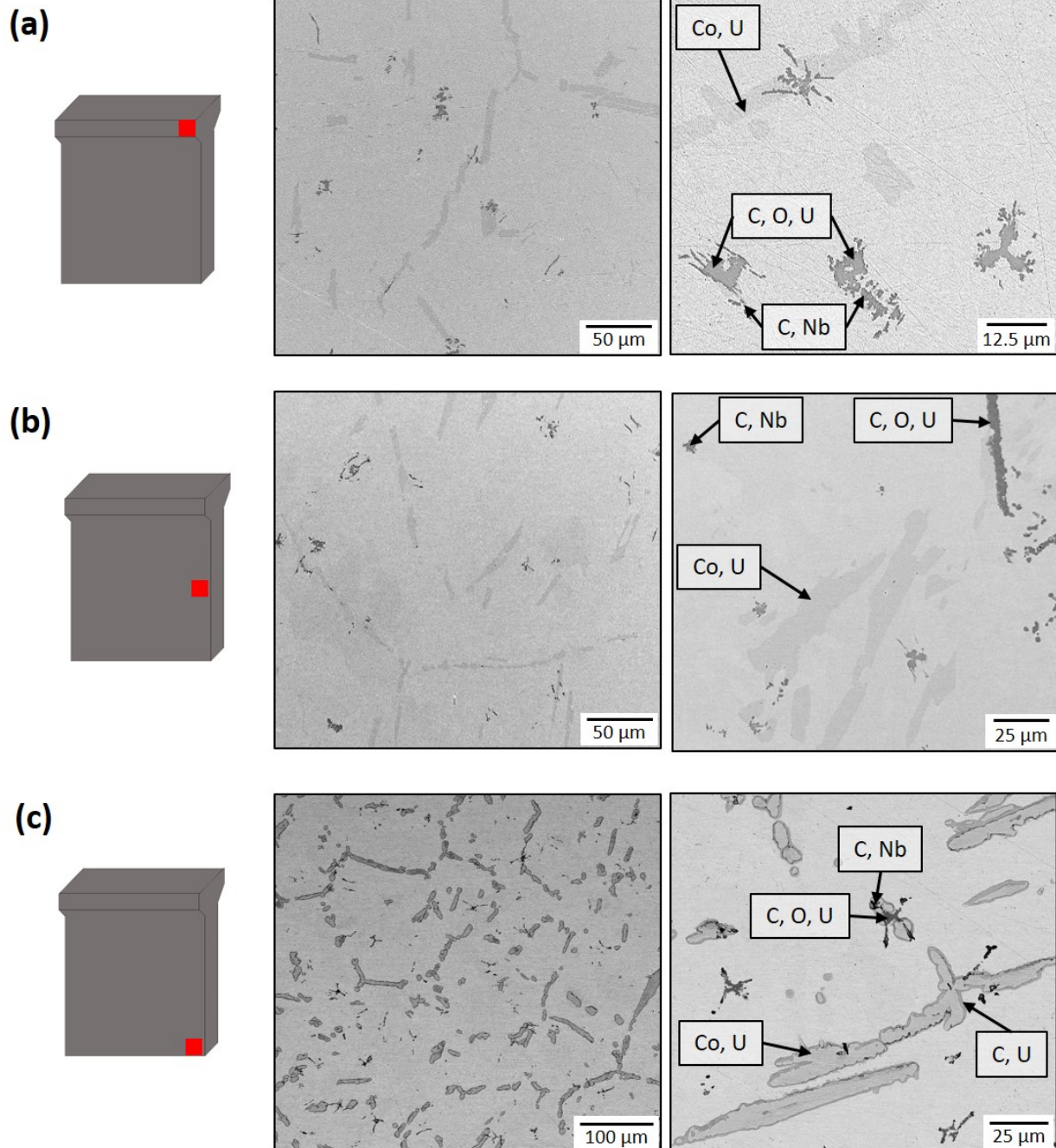


Figure 3.16. Representative BSE-SEM images taken from the (a) top, (b) middle, and (c) bottom of 20C1-080. Nb carbides and a Co-rich intermetallic phase were found throughout the casting. As with the baseline alloy that was used in the dilution, Ir and W were not found.

3.5.5. Conclusions – mixed/dilution alloys

Based on the chemistry and microstructure analysis from the mixed/dilution alloys, both bulk metal tagging strategies are still viable options for a majority of the taggant elements.

A majority of the elements are still viable options to be added as taggants to bulk uranium in specific ratios. Concerning detectability, the chemistry measurements of W and Ir differed between the two laboratories. If measurements are not repeatable between labs, the elements do not make suitable chemical taggants. Al and Au measured higher than expected which is unlikely to be a processing issue. Further investigation into the detection of these two elements should be done before choosing them as a chemical taggant. For manufacturability, there was no segregation between the top and the middle of each mixed/dilution alloy. The amount of the taggant that was measured compared to the calculated value looked much better in these alloys than they did in the baseline alloys. This strengthens the hypothesis that the low results in the baseline alloys was likely from poor mixing during processing. It is also likely that the majority of the taggant elements investigated can be added to uranium at a specified amount if care is taken to ensure proper mixing. However, this is likely not the case for Sc and Tb. These elements were measured at less than 15% of their expected value in all of the alloys so far. Unless more effort is spent investigating how to better incorporate them into uranium, these should not be considered for chemical taggants.

A majority of the elements are still options for second phase taggants as well. Similar to the baseline alloy, W was never positively identified via SEM/EDS. However, Ir was able to be located in the mixed alloys. V and Nb were both found, unexpectedly, in intermetallic phases. Also, the overlapping EDS peak with Nb and Au needs to be considered. All of these results show that care needs to be taken to fully characterize the second phases with any of the taggant elements chosen.

In summary, Sc, Tb, W, and Ir are unfit for chemical taggants while W is also unfit as a second phase taggant. However, if more time is spent looking into any of these options, that conclusion could change. The remaining eight elements, Al, Ti, V, Mn, Co, Nb, Pd, and Au, are still options as both chemical and second phase taggants.

3.6. FY21 activity – recycling study

3.6.1. Design and procedure

One important characteristic of a good elemental taggant in bulk uranium is that it will stick around through further material processing. To determine which of the chosen elements in this study would fill that criteria, a recycling study was designed to see if the taggants were still detectable through ICP-MS after being melted and cast multiple times. A schematic of the workflow is shown in **Figure 3.17**. The same material would be cast, sampled, and split to go through the process once again with no new material introduced throughout the study.

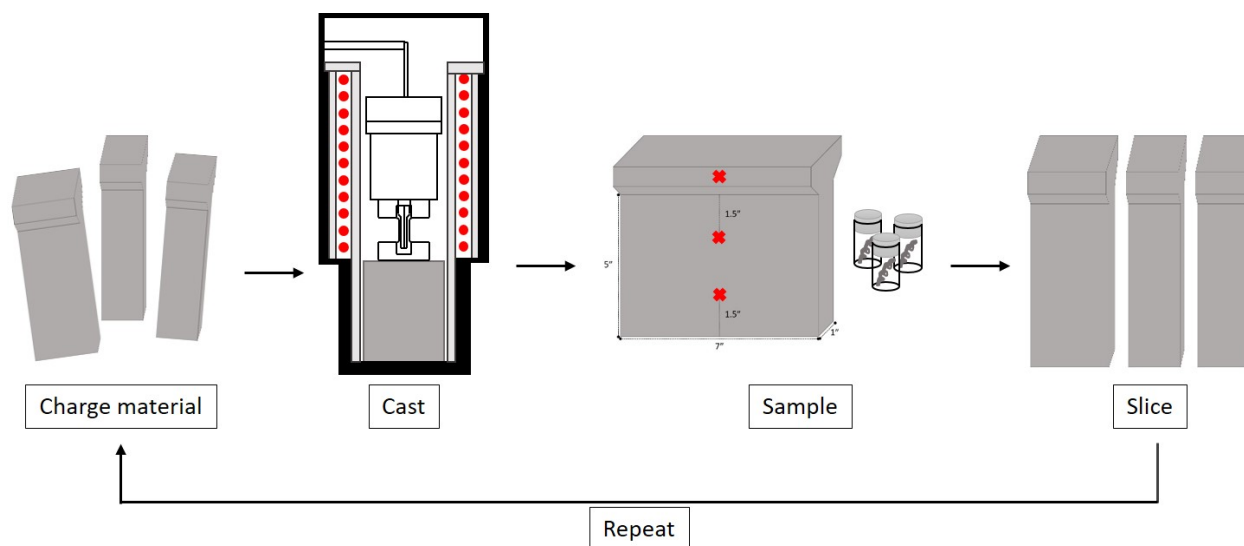


Figure 3.17. Schematic of the workflow for the recycling study.

The initial starting charge was a mix of the three successful baseline alloys: 4737 g from 19C1-010, 7751 g from 19C1-014, and 5489 g from 19C1-015. These three alloys were cast into a 5" tall, 7" wide, and 1" thick plate. The furnace setup and thermocouple locations are shown in **Figure 3.18**. After removal from the mold, three locations were sampled for chemical analysis: one from the top of the plate, one from 1.5" below the hot top, and one 1.5" up from the bottom of the plate. The sampled locations are illustrated in **Figure 3.17**. The as-cast plate was then sliced on a bandsaw to be used as charge material for the next casting. This was repeated for a total of ten castings, and details from each are shown in **Table 3.5**. All of the casting yields were above 96.90%, indicative of a successful campaign.

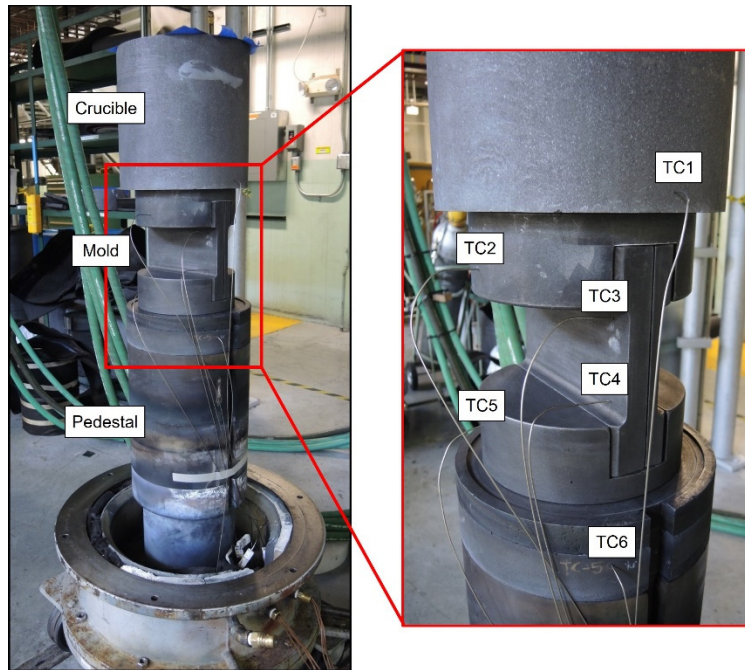


Figure 3.18. The furnace setup used in the recycling study showing the crucible, mold, and pedestal setup in the VIM furnace along with thermocouple (TC) locations.

Table 3.5. Casting details from the 10 plates. The high casting yields show it was a successful campaign.

Casting Number	Casting ID	Date Cast	Leak Rate (mTorr/min)	Charge mass (g)	As-cast mass (g)	Yield (%)	Cumulative mass loss (%)
1	21C1-105	03/09/21	5.48	17977	17431	96.96	3.037
2	21C1-107	03/11/21	5.52	17221	16708	97.02	7.059
3	21C1-109	03/15/21	8.76	16493	16328	99.00	9.173
4	21C1-111	03/18/21	5.46	16026	15560	97.09	13.44
5	21C1-112	03/23/21	5.32	15378	15064	97.96	16.20
6	21C1-113	03/26/21	5.30	14880	14455	97.14	19.59
7	21C1-114	03/30/21	5.62	14278	13881	97.22	22.78
8	21C1-115	04/01/21	5.40	13694	13269	96.90	26.19
9	21C1-116	04/06/21	5.18	13100	12735	97.21	29.16
10	21C1-118	04/09/21	7.68	12570	12290	97.77	31.63

A comparison of temperatures at the time of pour for each casting is shown in **Figure 3.19**. The melt temperature is read from an optical pyrometer pointed at the liquid metal, the top of the mold is TC3 in **Figure 3.18**, and the bottom of the mold is TC4 in **Figure 3.18**. As can be seen, most of the castings were very similar, but two of them were slightly different. Casting 3 and 10 both had stopper rods that were not properly seated. Stopper rods are used to plug the pour hole as the metal is melted and the mold is heated to a specific temperature profile. When specific temperatures are reached, the stopper rod is lifted, allowing the liquid metal to fill a warm mold. When the stopper rod is not seated properly, liquid metal leaks into a cold mold and quickly solidifies leading to large cold laps (i.e. metal freezing quickly enough at the surface that liquid streams freeze into distinct layers with seams and gaps), porosity, and void formation at the bottom of an as-cast part. In casting 3, the unseated stopper rod was noticed early in the run, so the metal was poured early into a mold colder than the goal, seen in **Figure 3.19**. Looking at all the as-cast plates in **Figure 3.20**, porosity at the bottom of casting 3, 21C1-109, is clearly visible. During casting 10, the unseated stopper rod was not noticed allowing a lot more of the metal to leak into a cold mold. This is extremely evident in the art-like quality of that final casting, 21C1-118 in **Figure 3.20**. However, since all the casting yields were okay, these mispoured castings should not affect the chemistry results. Also of note, there is a decreasing hot top height evident in **Figure 3.20**. Material will always be lost during casting, and if no new material is added, less metal ends up in the final part throughout the multiple castings runs.

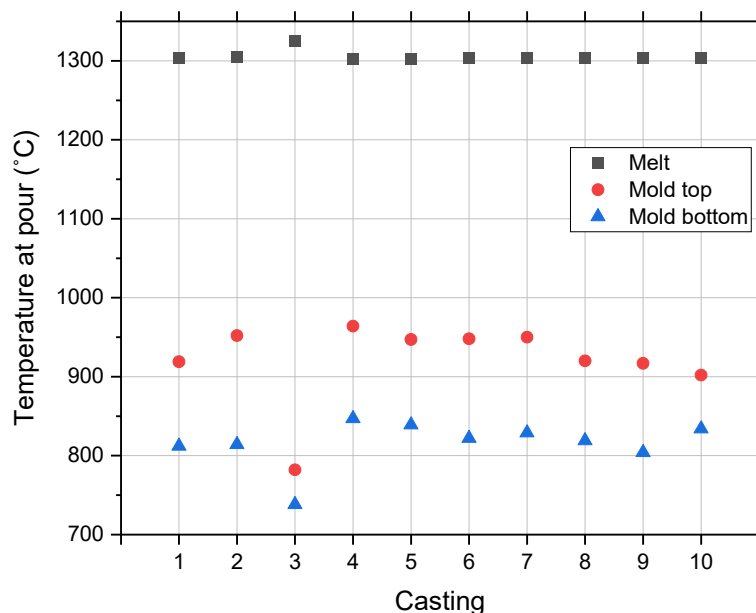


Figure 3.19. Temperatures at the time of pour for each casting in the recycling study. A majority of the runs were all poured at similar temperatures, but the early pour during casting 3 is evident.

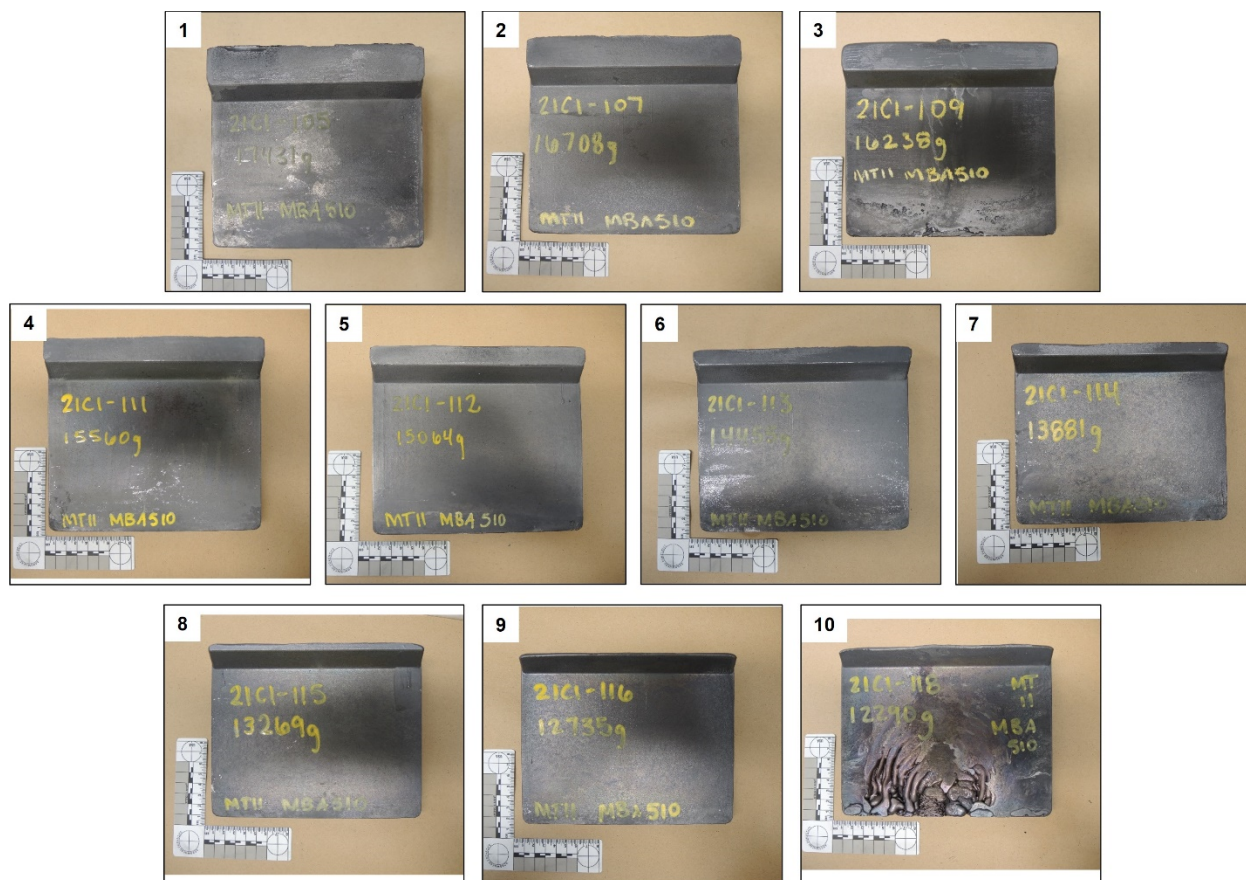


Figure 3.20. Photos of all the as-cast plates from the recycling study. The decreasing charge weights are evident in the decreasing height top height. Also, the porosity from the mispours on the third, 21C1-109, and the final, 21C1-118, castings are visible. This should not impact the chemistry results.

3.6.2. Retention of elements – chemistry results

One laboratory, Lab B, performed ICP-MS for bulk chemical analysis of the ten plates produced during the recycling study. **Figure 3.21** shows the chemistry measurements for each taggant element normalized to the calculated value for each casting. In other words, the plots show what percentage of the taggant element made it into the final part. The measured concentration values from the baseline alloys along with the initial charge weight was used to calculate the expected chemistry. The y-axis on each plot in **Figure 3.21** spans 100% with grid lines occurring every 20%, so while the numbers for each may be different, the scale stays the same for easy comparison between elements. In each plot, the green squares are measurements from the top of the plate, the red circles are from 1.5" down from the hot top, and the blue triangles are taken from 1.5" up from the bottom of each plate. The sample locations are shown schematically at the bottom of the figure.

The first and perhaps most important point is that only 1 of these 12 elements fell out of detection (Tb, which began at a very low level to begin with) even after 10 meltings, demonstrating their persistence. Recycling studies like this have not been reported in the

uranium literature, so we did not know quite what to expect going in. Uranium is a dense material, and flotation of second phases to the skull or hot top were certainly possible exit mechanisms for one or more elements, as is reaction with the crucible whose effects might accumulate after multiple melting runs even if they are not seen after one or two melts. Again, the continued presence of all the tagging elements after 10 melts is gratifying.

Sc and Tb both measure very low compared to their anticipated values, so much so that Tb was only detectable in the first casting. Recall, similar issues with Sc and Tb have been seen in the other castings throughout this project as well confirming that they should not be utilized as chemical taggants unless more work is done to determine better measurement tools or better ways to incorporate them into uranium metal. Al measured higher than expected, similar to previous castings. (Part of this can be explained by the unintended ~800 wppm level in one of the parent materials 19C1-010, which was not accounted for in the expected or calculated value.) The spread in measurements from the different locations in each plate is concerning since there seems to be no trend. Taking the average for each plate, it does appear that Al would remain consistent, but questions still remain. Ti is similar to Al except that it measures lower than expected. Again, questions would need to be answered before pursuing Al and Ti as chemical taggants. Nb also measured lower than expected, but it seems to be remaining consistent across all ten castings. Since Nb did not measure lower in the mixed/dilution castings, nothing definitive can be said. Pd and Au have a strange trend of decreasing until casting 6 where the measure values begin to increase above what was expected. While W seemed to remain constant, it did measure higher than expected. Ir also appeared to remain consistent, but there was a slightly larger spread in the values per casting than some of the other elements. Mn could be experiencing a slight decrease over the course of ten castings, but to determine if this trend is real, more castings would need to be carried out. V and Co both measured at their expected values, and both appear to remain constant across all ten castings.

3.6.3. Conclusions – recycling study

Ten cycles of melting and casting provided more insight into which elements would be suitable chemical taggants in bulk uranium. None of the 12 elements fell out of detection even after 10 meltings. Sc and Tb were still proving difficult to incorporate into uranium and can currently be ruled out as chemical taggant options. Nb did not appear to decrease across ten castings, but it did measure lower than expected. Since this was not an issue in the mixed/dilution castings, more time should be spent determining what occurred before it is ruled in or out as a chemical taggant. For the various reasons explained above, Al, Ti, Pd, W, Ir, and Au would also need to be studied more before a final decision was made. Mn could be experiencing a slight decrease over the ten castings, but more cycles would be needed to determine if this trend was real. V and Co showed no issues, making them ideal candidates for chemical tagging.

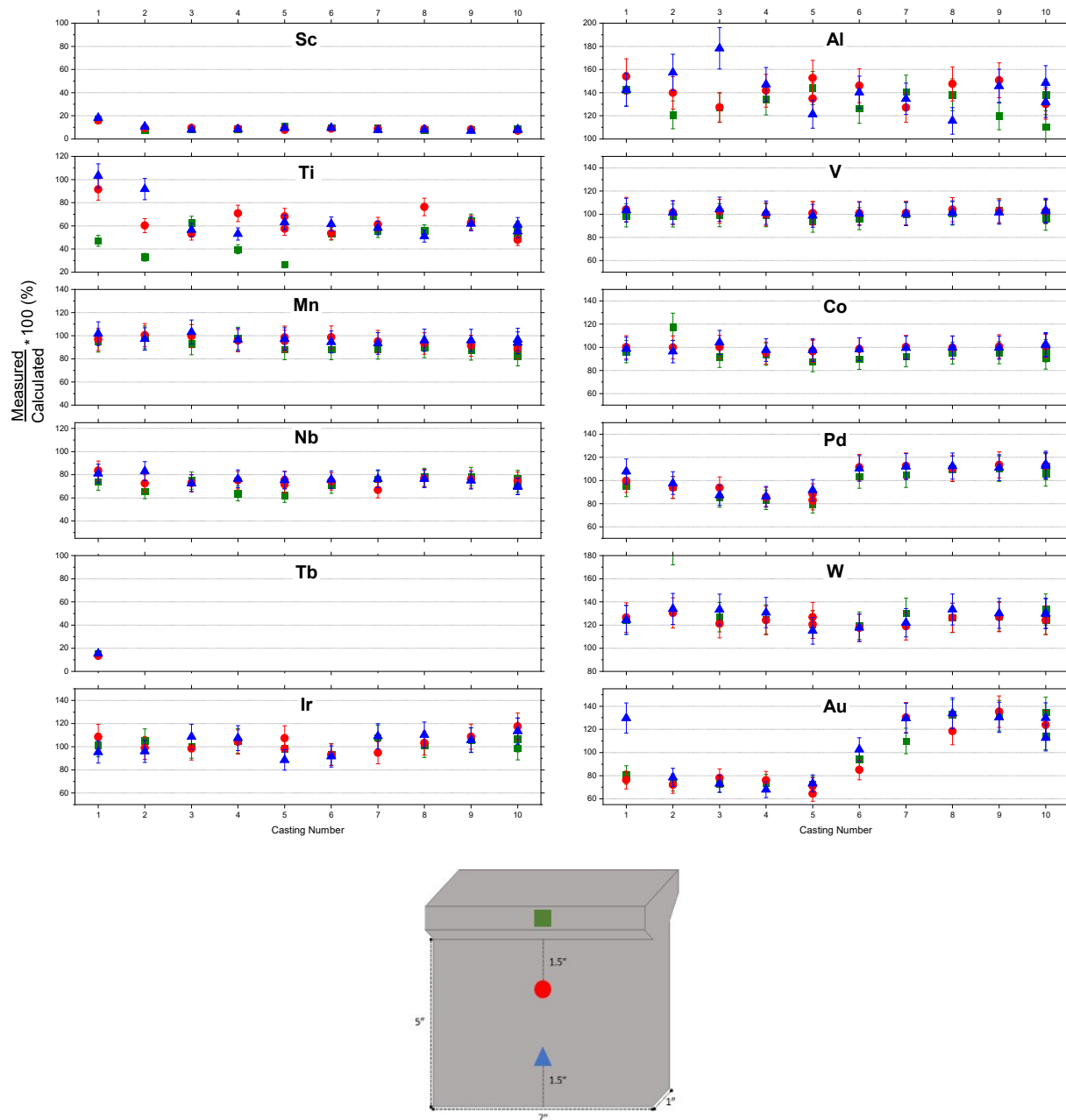


Figure 3.21. Chemistry measurements for each taggant element normalized to the calculated value for each casting. The three locations sampled per plate are schematically shown at the bottom of the figure.

3.7. Bulk metal tagging conclusions

To assess suitable taggant elements for bulk uranium metal, 18 castings were made and analyzed in this project: 4 baseline, 3 mixed, 1 dilution, and 10 recycled. With four elements removed due to processing issues, the remaining 12 elements were assessed to determine if

they would be suitable as a chemical and/or a second phase taggant in uranium. The results are summarized in a stoplight chart, **Table 3.6**. Conclusions regarding taggant acceptability and performance are determined based upon persistence and detectability. Any future use would require an assessment regarding the impact to material performance.

Table 3.6. Stoplight chart summarizing how each element would perform as either a chemical taggant or second phase taggant based on the current set of results.

Element		Tagging strategy	
Name	Symbol	Chemical Taggant	Second Phase Taggant
Aluminum	Al		
Scandium	Sc		
Titanium	Ti		
Vanadium	V		
Manganese	Mn		
Cobalt	Co		
Nickel	Ni		
Germanium	Ge		
Niobium	Nb		
Palladium	Pd		
Cerium	Ce		
Terbium	Tb		
Tantalum	Ta		
Tungsten	W		
Iridium	Ir		
Gold	Au		

Good choice
More work is needed
Should not be pursued without a lot more study
Downscoped from project due to processing issues

An element-by-element survey of the **suitability for chemical tagging** now follows. The “previous study” is referenced in [2013hac] (and the annual reports FY09-FY12 it cites which led to this final report.) The only metals chemical analyses in that study were from the two VIM castings of the same composition that contained (nominally) 0.05 wt.% each of Ti, V, and Mn, and 0.10 wt.% each of Zr, Mo, and Au. By way of preface, care needs to be taken during processing to ensure proper mixing any element chosen as a chemical taggant.

Two elements showed the **best results** (green in Table 3.6):

- V and Co
 - Detectable by two different laboratories.
 - Measured at their expected values after proper mixing during processing.
 - Remained at a consistent level through 10 casting cycles.
 - Good V result consistent with previous study.

Six elements, appearing as yellow in Table 3.5, showed **fair results** (yellow in Table 3.6) and need to be furthered studied before a decision should be made. The issues for these are:

- Al and Ti
 - Did not measure at their expected values.
 - Low Ti result is consistent with previous study.
 - Noticeable difference between the different locations per casting throughout the recycling study.
- Pd and Au
 - Unexplained trends in measured chemistry in the recycling study.
 - Au showed a good result (measured at or somewhat above nominal) in previous study.
- Nb
 - Measured lower than expected in the recycling study.
 - Measured at its expected value in the mixed/dilution castings.
- Mn
 - Could have slightly decreased over the course of ten castings, but to determine if this trend is real, more castings would need to be carried out.
 - Showed a good result (measured at nominal) in previous study.

Four elements (all red) showed the **poor results** (red in Table 3.6). Without a good deal more study, these should not be considered for chemical taggants

- Sc and Tb
 - Measured much lower than their calculated values
 - Could be a detection issue with ICP-MS
 - Could be a processing issue since these elements can be difficult to incorporate into uranium.
- W and Ir
 - Two laboratories did not agree on the measured values

It is of special note that in the recycling study only 1 of these 12 elements fell out of detection (Tb, which began at a very low level to begin with) even after 10 meltings, demonstrating their persistence.

Finally, four elements – Ni, Ge, Ce, Ta – are **inconclusive** (gray in Table 3.6), as their baseline casting had issues with a visible reaction in the crucible. It should be noted that in the previous NA-22 study by same PI [2013hac], all four of these elements were included in arc melted alloys, but resource limitations prevented their chemical analysis (apart from C, N, O analyses). Having said that, TEM was able to identify phases containing Ni, Ce, and Ta; Ge was not identified (intermetallics were expected) but that does not rule out its possible incorporation into alpha-uranium matrix or other second phases. So this indicates at least some amount of Ni, Ce, and Ta made it into the materials and could in addition be suitable for discreet second-phase tagging.

For **suitability for second-phase tagging**, six elements – Al, Ti, Mn, Co, Pd, and Tb – were able to be located in their expected phases via SEM-EDS and are considered good options for this tagging strategy. Five elements, Sc, V, Nb, Ir, and Au, were not always found in their anticipated second phase. These elements could still be viable second phase taggants as long as the alloy is fully and carefully characterized. Only one element, W, was not located in any of the alloys, and is therefore should not be pursued as a second phase taggant. And as mentioned in the preceding paragraph, Ni, Ge, Ce, and Ta were not further studied in this work, though the previous study found Ni, Ce, and Ta in second phase particles by TEM.

ACKNOWLEDGEMENTS

Cheryl Hawk, Andrew Duffield, and Stephen Wiest are acknowledged for their assistance with brainstorming and technical support. The entire foundry and solidification science team of Sigma Division is thanked for their help with the casting of all 18 bulk tagging alloys, especially Hunter Swenson, Ray Sandoval, Kaegan Schultz, Garry Sandoval, Anthony Florez, Eunice Solis, and Casey Shoemaker. We acknowledge Kevin Bohn for microscopy specimen preparation and the bulk chemical analysis work of Becky Chamberlin, Kevin Boland, Gabby Kral, Conor Emberley, Michael Rearick and Kevin Kuhn.

REFERENCES

- 2013hac R.E. Hackenberg, “Forensics and Safeguards of Uranium Metal Weaponization: Final Project Report,” report LA-CP-13-00583, Los Alamos National Laboratory, Los Alamos, NM (9 May 2013). From NA-22 project LA09-WPT260-PD04. OUO.
- 2019hac R.E. Hackenberg, T.J. Baker, A.N. Black, J.S. Carpenter, J.C. Cooley, S.D. Imhoff, J.J. Lopez, K.E. Luitjohan, E.P. Luther, C.J. Montgomery, J.A. Stull, and E.L. Tegtmeier “Intentional Uranium Tagging for Material Provenance and Pathway Forensics (LA19-Intentional-Forensics-NDD3Bb): Annual Report for FY19,” Los Alamos National Laboratory, report LA-CP-19-20691 (October 2019), 57 pp. OUO.
- 2020hac R.E. Hackenberg, A.N. Black, S.D. Imhoff, K.E. Luitjohan, C.J. Montgomery, L.B. O’Brien, and E.L. Tegtmeier “Intentional Uranium Tagging for Material Provenance and Pathway Forensics (LA19-Intentional-Forensics-NDD3Bb): Annual Report for FY20,” Los Alamos National Laboratory, report LA-CP-20-20637 (October 2020), 40 pp. OUO.

2021blo R. Bloom, "Photoluminescence in Tagging: A Glowing Review," report LA-UR-21-31632, Los Alamos National Laboratory (November 2021), 19 pp.
doi.org/10.2172/1833235

APPENDIX: Chemical analysis results for the 18 bulk tagging alloys.

The following tables present the measured chemistry values of all 18 alloys processed in this study. Lab A returned the values with three significant figures while measurements from Lab B were truncated at four significant figures. All results are in wppm unless otherwise indicated.

19C1-010 : baseline alloy (wppm)					
Element	Calculated	Lab A hot top	Lab A mid-plate	Lab B mid-plate	Lab B mid-plate
Al				745.7	888.5
Sc				12.10	11.10
Ti	4982	2750	2440	2698	2676
V				6.212	10.40
Mn	5035	3720	3300	3278	3284
Co				6.822	174.3
Ni				11.50	12.50
Cu				44.10	46.10
Ge				4.180	4.206
Y				1.733	2.152
Nb				1.994	2.980
Pd				30.90	30.00
Ce				0.3639	0.4996
Tb	4801	85.7	81.5	89.60	86.60
W				45.30	802.5
Ir				2.691	0.03031
Au	4994	718	589	739.0	713.9

19C1-014 : baseline alloy (wppm)				
Element	Calculated	Lab A hot top	Lab A mid-plate	Lab B mid-plate
Al	4895	2310	2120	2242
Sc	4884	243	268	289.2
Ti				26.60
V	4889	4270	3990	4068
Mn				14.30
Co				3.130
Ni				11.10
Cu				45.70
Ge				4.312
Y				8.876
Nb				0.867
Pd	4642	720	658	718.2
Ce				0.4440
Tb				2.818
W				24.90
Ir				
Au				14.10

19C1-015 : baseline alloy (wppm)					
Element	Calculated	Lab A hot top	Lab A hot top	Lab A mid-plate	Lab B mid-plate
Al					16.20
Sc					5.216
Ti					10.60
V					3.650
Mn					12.60
Co	5000	4140	4200	4600	4185
Ni					20.80
Cu					50.00
Ge					4.154
Y					1.483
Nb	4995	3910	3770	3830	3465
Pd					9.921
Ce					0.3963
Tb					6.639
W	5006	787	818	745	745.6
Ir	3630	3080	3100	3190	2754
Au					15.20

19C1-016 : baseline alloy (wppm)					
Element	Calculated	Lab A hot top	Lab A mid-plate	Lab B mid-plate	Lab B mid-plate
Al				75.10	46.90
Sc				4.650	8.359
Ti				21.50	20.50
V				4.973	7.723
Mn				12.60	14.30
Co				28.80	7.625
Ni	4982	4650	4750	4579	4699
Cu				46.10	72.50
Ge	5094	1540	1430	1449	1449
Y				1.649	2.476
Nb				1.496	4.938
Pd				19.70	23.90
Ce	5012	693	713	611.5	615.8
Tb				1.431	2.475
Ta	5000	412	400		
W				329.0	31.70
Ir					10.80
Au				14.30	14.30

20C1-076 : mixed alloy (wppm)					
Element	Calculated	Lab A hot top	Lab B hot top	Lab A mid-plate	Lab B mid-plate
Al	1108	1270	1330	1230	1244
Sc	125.9	18.0	12.10	14.0	18.10
Ti		8.45	15.20	8.67	25.90
V	2091	2150	2082	2070	2036
Mn		24.0	13.20	15.4	13.60
Co	2184	2180	2080	2420	2022
Ni		17.7	15.20	12.2	14.70
Cu			48.10		489.6
Ge			4.551		4.231
Y			2.776		5.956
Nb	1886	1760	1709	1760	1645
Pd	352.6	357	378.7	341	374.0
Ce			0.3560		0.3894
Tb		0.180	1.157	0.150	1.310
Ta		1.33		1.09	
W	372.2	523	368.5	516	362.7
Ir	1563	1620	1385	1580	1373
Au		247	11.40	154	11.90

20C1-077 : mixed alloy (wppm)						
Element	Calculated	Lab A hot top	Lab B hot top	Lab A mid-plate	Lab B mid-plate	Lab B mid-plate
Al	1095	1610	1455	1580	1518	1485
Sc	124.4	3.17	4.103	5.19	9.562	8.483
Ti	1306	1300	1350	1340	1366	1340
V	2066	1930	1959	1970	1993	2043
Mn	1758	1640	1475	1700	1621	1693
Co		0.830	3.064	2.18	3.092	4.799
Ni		5.87	9.965	7.82	10.80	11.70
Cu			42.20		43.40	43.50
Ge			4.326		4.140	4.259
Y			1.372		2.469	2.186
Nb		1.64	2.725	2.91	2.348	1.255
Pd	348.4	351	365.5	365	382.0	392.7
Ce			0.3605		0.3407	0.3936
Tb	50.20	0.640	1.657	1.21	3.354	3.106
Ta		0.660		0.670		
W		9.05	6.059	7.64	4.834	15.90
Ir		2.50		1.46		
Au	326.5	435	364.9	429	375.1	387.3

20C1-078 : mixed alloy (wppm)					
Element	Calculated	Lab A hot top	Lab B hot top	Lab A mid-plate	Lab B mid-plate
Al		404	380.6	355	409.7
Sc		1.84	3.541	1.69	3.199
Ti	1296	1140	1075	996	1083
V		16.4	4.942	12.1	4.972
Mn	1744	1670	1547	1650	1709
Co	2207	1910	1898	1910	2136
Ni		13.0	15.80	9.46	17.10
Cu			45.50		47.10
Ge			4.496		4.120
Y			4.143		1.505
Nb	1906	1800	1689	1620	1684
Pd		18.5	20.40	16.3	21.20
Ce			0.3443		0.3644
Tb	49.80	1.10	5.353	2.56	2.850
Ta		1.09		1.03	
W	376.2	543	393.2	578	381.5
Ir	1580	1970	1431	2040	1459
Au	324.0	437	380.1	389	387.0

20C1-080 : dilution alloy (wppm)					
Element	Calculated	Lab A hot top	Lab B hot top	Lab A mid-plate	Lab B mid-plate
Al			59.10		27.20
Sc		1.36	3.229	1.25	3.123
Ti		14.3	18.80	8.23	24.80
V		21.8	3.473	33.6	3.531
Mn		9.32	12.00	9.40	9.741
Co	2198	2000	1948	2070	2041
Ni		15.0	17.60	14.5	19.20
Cu			43.70		49.60
Ge			3.963		4.267
Y			1.404		2.263
Nb	1899	1870	1791	1880	1752
Pd		4.47	7.106	4.56	6.404
Ce			0.3504		0.3736
Tb		0.190	1.195	0.0980	1.139
Ta		0.860		0.850	
W	374.7	547	371.1	542	377.7
Ir	1574	2010	1411	2110	1468
Au		105	12.00	28.1	8.476

21C1-105 : recycle casting 1 (wppm)				
Element	Calculated	Lab B hot top	Lab B mid-plate	Lab B bottom
Al	949.0	1355	1460	1351
Sc	108.0	18.10	17.20	19.60
Ti	685.0	322.4	626.3	707.4
V	1789	1771	1863	1852
Mn	922.0	878.9	893.1	938.4
Co	1344	1294	1345	1327
Nb	1160	857.0	967.7	939.7
Mo	0	17.40	14.30	14.00
Pd	302.0	288.8	300.9	325.5
Tb	26.00	4.015	3.549	4.062
Yb	0	2.845	2.831	2.949
Hf	0	16.40	14.60	14.50
Ta	0	23.50	22.20	21.00
W	229.0	285.4	289.8	285.0
Ir	962.0	976.3	1043.6	917.1
Au	171.0	138.0	130.7	222.3

21C1-107 : recycle casting 2 (wppm)			
Element	Lab B hot top	Lab B mid-plate	Lab B bottom
Al	1146	1326	1493
Sc	8.343	10.20	11.50
Ti	224.9	412.9	628.9
V	1770	1814	1818
Mn	909.6	926.4	896.6
Co	1581	1342	1294
Nb	765.1	842.0	962.4
Mo	13.60	12.20	12.90
Pd	283.8	283.5	294.9
Tb	< 10.00	< 10.00	< 10.00
Yb	3.018	3.411	2.736
Hf	14.30	14.20	13.60
Ta	19.80	19.00	18.50
W	437.7	298.9	306.9
Ir	1009.2	951.8	924.3
Au	127.0	123.5	134.5

21C1-109 : recycle casting 3 (wppm)			
Element	Lab B hot top	Lab B mid-plate	Lab B bottom
Al	1204	1208	1690
Sc	9.011	10.30	8.689
Ti	425.5	363.9	386.9
V	1774	1836	1867
Mn	856.0	918.7	951.7
Co	1233	1346	1400
Nb	869.6	844.8	841.7
Mo	11.60	12.60	12.20
Pd	258.0	283.0	263.3
Tb	< 10.00	< 10.00	< 10.00
Yb	2.822	2.821	2.757
Hf	13.60	13.90	13.50
Ta	18.00	18.10	17.40
W	290.6	277.5	305.5
Ir	962.6	947.0	1044.5
Au	125.0	133.8	125.0

21C1-111 : recycle casting 4 (wppm)			
Element	Lab B hot top	Lab B mid-plate	Lab B bottom
Al	1273	1344	1395
Sc	8.833	9.618	9.140
Ti	272.3	485.0	363.2
V	1774	1790	1812
Mn	901.1	882.9	891.1
Cu	59.30	69.80	59.50
Co	1261	1277	1311
Nb	741.6	871.5	886.3
Mo	12.00	12.30	12.10
Pd	251.4	258.1	260.3
Tb	< 10.00	< 10.00	< 10.00
Yb	2.778	2.905	2.768
Hf	13.80	13.90	13.70
Ta	17.30	17.80	17.40
W	286.2	284.3	299.6
Ir	1010	1002	1034
Au	126.2	130.2	116.4

21C1-112 : recycle casting 5 (wppm)				
Element	Lab B hot top	Lab B mid-plate	Lab B mid-plate (replicate)	Lab B bottom
Al	1366	1448	1279	1151
Sc	11.70	9.456	8.476	10.20
Ti	180.7	394.2	467.0	431.8
V	1680	1805	1803	1768
Mn	812.6	907.8	878.6	896.2
Cu	56.40	61.10	58.80	64.00
Co	1178	1301	1295	1311
Nb	722.4	873.2	829.9	874.5
Mo	12.70	12.40	12.60	19.80
Pd	241.0	266.6	250.4	276.7
Tb	< 10.00	< 10.00	< 10.00	< 10.00
Yb	2.774	2.754	2.784	2.899
Hf	13.90	13.50	13.60	16.40
Ta	17.00	16.80	17.00	26.40
W	276.0	290.7	276.0	263.5
Ir	942.4	1032	944.5	852.2
Au	123.6	121.8	110.4	125.7

21C1-113 : recycle casting 6 (wppm)			
Element	Lab B hot top	Lab B mid-plate	Lab B bottom
Al	1196	1384	1330
Sc	10.20	9.607	10.30
Ti	363.0	367.3	421.6
V	1722	1806	1797
Mn	812.4	909.4	872.7
Cu	58.00	62.00	83.20
Co	1208	1322	1321
Nb	824.4	862.6	879.4
Mo	15.80	14.30	17.10
Pd	312.6	336.1	333.1
Tb	< 10.00	< 10.00	< 10.00
Yb	2.846	2.843	2.881
Hf	14.80	14.40	14.50
Ta	23.60	22.00	20.90
W	273.7	269.3	269.7
Ir	898.2	896.1	881.3
Au	161.5	145.7	175.8

21C1-114 : recycle casting 7 (wppm)			
Element	Lab B hot top	Lab B mid-plate	Lab B bottom
Al	1337	1206	1278
Sc	9.820	9.325	8.294
Ti	379.6	419.5	398.6
V	1792	1810	1795
Mn	817.2	876.6	861.4
Cu	60.00	61.30	65.00
Co	1240	1347	1337
Nb	881.0	774.9	886.4
Mo	13.40	13.50	12.90
Pd	315.5	339.8	338.0
Tb	< 10.00	< 10.00	< 10.00
Yb	2.833	2.827	2.891
Hf	14.20	14.20	14.30
Ta	20.30	19.10	19.20
W	298.5	272.6	279.3
Ir	1037.8	911.9	1048.5
Au	188.5	223.0	222.1

21C1-115 : recycle casting 8 (wppm)			
Element	Lab B hot top	Lab B mid-plate	Lab B bottom
Al	1310	1399	1097
Sc	8.313	9.367	8.665
Ti	379.7	522.8	349.9
V	1802	1861	1815
Mn	831.0	861.6	885.6
Cu	60.90	65.70	79.50
Co	1277	1339	1342
Nb	902.9	892.6	887.4
Mo	12.90	12.10	12.00
Pd	332.2	333.1	339.1
Tb	< 10.00	< 10.00	< 10.00
Yb	2.821	2.858	2.841
Hf	14.10	14.20	14.10
Ta	18.90	18.30	18.20
W	288.9	289.6	305.8
Ir	970.6	992.9	1060.8
Au	227.0	203.0	229.4

21C1-116 : recycle casting 9 (wppm)			
Element	Lab B hot top	Lab B mid-plate	Lab B bottom
Al	1138	1429	1381
Sc	8.678	8.992	7.608
Ti	437.2	429.6	423.7
V	1843	1843	1817
Mn	807.9	842.6	884.3
Cu	61.90	66.20	63.30
Co	1280	1353	1339
Nb	909.8	882.7	871.1
Mo	17.20	14.10	13.60
Pd	332.8	342.5	335.5
Tb	< 10.00	< 10.00	< 10.00
Yb	2.846	2.859	2.843
Hf	16.40	14.70	14.40
Ta	24.00	21.70	20.50
W	292.1	290.9	298.1
Ir	1015	1045	1018
Au	225.8	231.8	223.4

21C1-118 : recycle casting 10 (wppm)					
Element	Lab B hot top	Lab B hot top (replicate)	Lab B mid-plate	Lab B bottom	Lab B bottom (replicate)
Al	1043	1309	1234	1408	1249
Sc	8.993	9.400	7.648	8.334	9.009
Ti	398.4	355.0	328.2	379.1	418.3
V	1713	1825	1833	1852	1838
Mn	757.8	813.8	819.0	866.7	892.1
Cu	63.40	135.90	68.60	69.40	157.10
Co	1213	1304	1357	1377	1366
Nb	839.3	883.4	866.7	812.5	808.6
Mo	12.40	12.80	12.70	12.60	13.00
Pd	318.8	337.7	340.1	340.2	343.8
Tb	< 10.00	< 10.00	< 10.00	< 10.00	< 10.00
Yb	2.873	2.866	2.861	2.827	2.856
Hf	14.30	14.30	14.20	14.20	14.20
Ta	19.60	19.30	18.60	18.10	18.50
W	284.4	305.8	284.5	298.2	297.5
Ir	948.7	1022	1130	1091	1092
Au	195.1	230.3	212.3	193.0	222.6